AD-A177 070

REPORT DOCUMENTATION PAGE

1a. REPORT SECURITY CLASSIFICATION Unclassified	1b. RESTRICTIVE MARKINGS
2a. SECURITY CLASSIFICATION AUTHORITY	3. DISTRIBUTION/AVAILABILITY OF REPORT
2b. DECLASSIFICATION/DOWNGRADING SCHEDULE	Unlimited
4. PERFORMING ORGANIZATION REPORT NUMBER(S) 1	5. MONITORING ORGANIZATION REPORT NUMBER(S) AFOSR-TR- 87 0085

6a. NAME OF PERFORMING ORGANIZATION Electrical & Computer Engrg. Carnegie Mellon University	6b. OFFICE SYMBOL (If applicable)	7a. NAME OF MONITORING ORGANIZATION Air Force Office of Scientific Research
6c. ADDRESS (City, State and ZIP Code) Pittsburgh, PA 15213		7b. ADDRESS (City, State and ZIP Code) Bolling Air Force Base Washington, DC 20332
8a. NAME OF FUNDING/SPONSORING ORGANIZATION AFOSR/NE	8b. OFFICE SYMBOL (If applicable)	9. PROCUREMENT INSTRUMENT IDENTIFICATION NUMBER AFOSR-84-0341

8c. ADDRESS (City, State and ZIP Code) Bolling Air Force Base Washington, D.C. 20332	10. SOURCE OF FUNDING NOS.			
	PROGRAM ELEMENT NO. 61102F	PROJECT NO. 2305	TASK NO. C1	WORK UNIT NO.

11. TITLE (Include Security Classification) (unclassified) Design & Fabrication of Submicron Magnetic Bubble Device Technology

12. PERSONAL AUTHOR(S) M.H. Kryder, M. Alex, C.L. Bauer, R.O. Campbell, D.W. Greve, A. Guzman, S. Jo, P.H.L. Rasky, M. Ramesh, J.F. Silvain, J. Wullert

13a. TYPE OF REPORT Final Scientific	13b. TIME COVERED FROM 9/30/84 TO 9/29/86	14. DATE OF REPORT (Yr., Mo., Day) Oct. 31, 1986	15. PAGE COUNT 66

16. SUPPLEMENTARY NOTATION

17. COSATI CODES			18. SUBJECT TERMS (Continue on reverse if necessary and identify by block number)
FIELD	GROUP	SUB. GR.	Bubble Memory; Ion Implantation; Garnet; Silicon-on-Insulator; Silicon-on-Garnet.

19. ABSTRACT (Continue on reverse if necessary and identify by block number)

Work was carried out on high density (16 to 64 Mbit/cm^2) magnetic bubble device technology. Highlights of the research include the successful fabrication of silicon MOSFETS on bubble garnet substrates and the development of ion implanted bubble devices utilizing 0.5µm bubbles in garnets with isotropic magnetostriciton. In addition, studies of the effects of ion implantation on garnet lead to improved fabrication techniques for the 0.5µm devices. Chips utilizing 1µm bubbles were demonstrated to have about 9% bias field margins at 50 Oe drive, and a numerical model was developed to model current accessed ion implanted devices.

DTIC FILE COPY

20. DISTRIBUTION/AVAILABILITY OF ABSTRACT UNCLASSIFIED/UNLIMITED ☒ SAME AS RPT. ☐ DTIC USERS ☐	21. ABSTRACT SECURITY CLASSIFICATION Unclassified
22a. NAME OF RESPONSIBLE INDIVIDUAL Dr. Gerald Witt	22b. TELEPHONE NUMBER (Include Area Code) 767-4931	22c. OFFICE SYMBOL NE

DD FORM 1473, 83 APR   EDITION OF 1 JAN 73 IS OBSOLETE.

SECURITY CLASSIFICATION OF THIS PAGE

Design and Fabrication of Submicron
Magnetic Bubble Device Technology

M. H. Kryder, M. Alex, C. L. Bauer, R. O. Campbell,
D. W. Greve, A. M. Guzman, S -C. Jo, P.H.L. Rasky and M. Ramesh,
J-F. Slvain and J. Wullert

Magnetics Technology Center
Carnegie Mellon University

Final Scientific Report

Executive Summary

During the period September 30, 1984 to September 29, 1986 work was carried out at Carnegie Mellon University under AFOSR grant number 84-0341 on the design and fabrication of submicron magnetic bubble device technology. Two results from the research have been classified as major accomplishments. Our successful fabrication of silicon MOSFETS on magnetic bubble garnet substrates was selected by Science Digest (December, 1985) to be one of the "Top 100 Innovations" in 1985 and has the potential of leading to much faster access time data storage devices. Our development of magnetic garnet materials with isotropic magnetostriction has furthermore resulted in dramatic improvements in the operating margins of ion implanted contiguous disk bubble devices utilizing 0.5μm diameter bubbvles. These new materials make possible chip capacities as large as 64 megabits.

In addition to the above two major accomplishments, we also made significant progress in a number of other areas.

In studies of the effects of ion implantation on garnet we used electron microscopy to study how high dose implantation leads to damage in the single cyrstal garnet and how photolithography and ion implantation conditions affect the strain contours at pattern edges in ion implanted bubble devices. From this wrok we now understand the limitations which the ion implantation process places on the bit density of ion implanted bubble devices, and have been able to develop processes which make it possible to make devices utilizing 0.5μm diameter bubble domains.

In studies of ion implanted device design, we obtained overlapping bias field margins of about 9% for all functions on a chip with 50 Oe drive field applied. Minor improvements to the gate design used for transferring data into the minor loops would improve this to more than 10%. These margins are comparable to those of much lower density devices in production today.

87   2 20 142

In studies of current-access ion implanted technology we developed numerical modeling tools which can be used for the development of new higher data rate current-accessed devices. Comparisons of the model with experimental data indicate a good fit. If these devices are successful, the data rate of bubble devices could be increased by an order of magnitude.

Detailed descriptions of the above research are contained in the attached reports, many of which have appeared as journal publications.

Accession For	
NTIS GRA&I	☒
DTIC TAB	☐
Unannounced	☐
Justification	
By	
Distribution/	
Availability Codes	
Dist	Avail and/or Special
A-1	

DTIC
COPY
INSPECTED
6

Integrated Silicon on Garnet Device Structures

P.H.L. Rasky, D.W. Greve. and M.H. Kryder

Department of Electrical and Compu. ̄ngineering, Carnegie Mellon

ABSTRACT

Silicon MOSFETs have been fabricated on magnetic bubble substrates. These devices are separated from the bubble film by one or more spacer layers. If a single SiO_2 spacer is used, high gate leakage occurs; I_G is usually greater than $1\mu A$ at $V_{GS}=1V$ for $V_{DS}=0V$. When a double spacer of SiO_2 and Si_3N_4 is used, the gate leakage current is low; typically, $I_G < 100pA$ at $V_{GS}=4V$ for $V_{DS}=0V$. We have found that the present silicon on garnet fabrication process does alter the room temperature magnetic properties of the bubble substrate. The saturation magnetization drops by 20% for $1\mu m$ material, and by 14% for $0.5\mu m$ material. However, it may be possible to reverse these changes by a suitable post-process anneal. Oxygen anneals near the growth temperature of the ₀ubble film have been effective thus far. Silicon magnetodiodes have been fabricated on silicon substrates with sensitivities of 2.1×10^{-4} $\mu A/Gauss$ per μm of diode width at $V_{diode}=30.0V$. This represents the first step toward our goal of fabricating integrated silicon on garnet magnetic field sensors.

INTRODUCTION

Magnetic bubble memories/systems are of current interest for a number of reasons. They are inherently non-volatile and radiation hard, two particularly important features when equipment, such as satellites, must operate for long periods of time in harsh electromagnetic environments. Unfortunately, large bubble systems have long data access times .- it takes tens of milliseconds for querying subsystems to get the information they seek. Shorter access times are clearly desirable, and our research indicates that it may be possible to significantly reduce the access time by utilizing integrated bubble/semiconductor devices.

Conceptually our solution is simple: use many small (high sensitivity) magnetic bubble sensors instead of one very large (low sensitivity) detector and multiplex the output data before it's taken off chip. The multiplexing can be done with MOSFETs, and the detection can be done with high sensitivity silicon magnetodiodes. The number of sensors used could be 1000 or larger.

Figures 1 and 2 show a magnetodiode sensor integrated with an ion-implanted propagation pattern. In this design, magnetic bubbles move along the propagation pattern in response to a rotating in-plane magnetic field until they reach the hairpin stretcher. The hairpin stretcher is then activated by applying a large current pulse (100-200mA), causing the effective bias field in the ion-implanted channel to be lowered. The bubble therefore expands into the channel, and part of its flux is intercepted by the silicon magnetodiode. This flux will deflect electrons and holes to one of the interfaces. Which interface they are deflected to will depend on the field's orientation ($F = qV \times B$). When these current carriers arrive at an interface, they will recombine at a rate dependent on the surface recombination velocity (S) of the interface. In general, each interface has a different S and one therefore expects the density of free electrons and holes in the base region (n- Si) to change. A change in electron - hole density implies a chance in conductivity and consequently a change in diode current for a fixed voltage across the diode. Figure 3 illustrates how this effect can be utilized in practice. For the $B > 0$ case, some electrons (and holes) that would recombine at the high S interface (the bottom interface) are deflected toward the low S interface (the top interface), and the diode current increases since more electrons and holes are available to participate in the conduction process.

DEVICE CHARACTERISTICS: MAGNETODIODES

Silicon magnetodiodes have been fabricated on silicon substrates, and the structure of these diodes is shown in Fig. 4(A). The current - voltage characteristics of our devices were similar to those of other researchers [1]. Figure 4(B) shows the diode current (for a fixed voltage of +30 volts) when the in-plane B field is swept between + and - 16kG. From this data, it follows that the diode has a sensitivity of 2.1E-4 μA/Gauss per μm of diode width. Furthermore, the qualitative behavior of the diode current agrees with that expected from the simple theory introduced in the preceding section. When +B is applied (see Fig. 4(C)), the Lorentz force deflects electrons and holes to the top interface and the diode current increases. When -B is applied, $qV \times B$ deflects electrons and holes to the bottom interface and the diode current decreases.

DEVICE CHARACTERISTICS: MOSFETS

In this section, we report on the device characteristics of silicon on garnet MOSFETs. We will show that devices fabricated on garnet wafers with $SiO_2 + Si_3N_4$ spacer layers are of higher quality than those fabricated on substrates coated with only SiO_2.

Figure 5 shows the final cross section for a silicon on garnet FET. In this case, the single SiO_2 spacer was deposited by RF sputtering and is $1\mu m$ thick. On top of the oxide spacer, a 0.5 - 0.75 μm LPCVD polysilicon film was deposited at 625°C and 0.4 torr. The poly Si was capped with $1\mu m$ of sputtered silicon dioxide, recrystallized with an Argon laser, and patterned into 25 x 100 μm islands. The islands were doped via ion-implantation and a $0.1\mu m$ gate oxide was grown in wet oxygen at 850°C. After opening contact windows, aluminum was deposited and patterned to form the source, drain, and gate electrodes.

Current - voltage characteristics for MOSFETs fabricated on SiO_2 coated bubble substrates fall into two basic categories: (1), devices with gate current less than the drain current (Fig. 6(A)), and (2), devices with gate current greater than the drain current (Fig. 7(A)). The corresponding low and high gate leakage models are given in Fig. 6(B) and 7(B). In the later case, the gate leakage current is so high that formation of an inversion layer is not possible. This is not the case for the first model, and one may verify the correctness of these models by using simple circuit analysis. From the model of Fig. 6(B), we find $I_D < 0$ for $V_{DS} < [R_S/(R_S + R_{OX})]V_{GS}$ and $I_D > 0$ for $V_{DS} > [R_S/(R_S + R_{OX})]V_{GS}$. By inspection, we find $I_D = 0$ when $V_{GS} = V_{DS}$ for the model of Fig. 7(B). These non-ideal characteristics can be attributed to contamination of the silicon island and gate oxide [2].

Next, MOSFETs with the structure shown in Fig. 8 were fabricated. In this case, both the SiO_2 and Si_3N_4 spacers were deposited by LPCVD. The oxide was deposited at 860°C by reacting SiH_4 and N_2O. The Si_3N_4 was deposited at 800°C by reacting SiH_4 and NH_3. LPCVD was selected since this technique is known to produce high quality layers.

Figure 9 shows a I-V characteristic for a device with the structure shown in Fig. 8 - note the absence of negative drain current for small positive V_{DS} for all V_{GS} (cf. with Fig. 6(A)). The improvement over the single oxide spacer case can be made even more clear by comparing the I_G vs. V_{GS} plots for devices fabricated on SiO_2 and SiO_2 + Si_3N_4 spacers - see Fig. 10 and 11. At $V_{GS} = 3.0$ V, the device fabricated on the double spacer layer (SiO_2 + Si_3N_4) has a gate leakage current six orders of magnitude lower than the device fabricated on the single SiO_2 spacer layer. The breakdown

characteristic for the double spacer layer device is also substantially sharper than for the single spacer layer device. We have also found that a thinner (0.24 μm) Si_3N_4 spacer is just as effective in reducing contamination, and hence gate leakage, as is the thick (0.85 μm) nitride spacer.

STABILITY OF MAGNETIC BUBBLE FILMS: ANNEALING

The data presented thus far indicates that fabrication of silicon on garnet devices is possible, but the issue of what the requisite high temperature processing does to the magnetic properties of the bubble film still must be addressed. Table 1 lists measured values for the saturation magnetization $4\pi M_s$ and zero field strip width W_o after each of the processing steps (with the exception of the gate oxidation step) used to fabricate the structure shown in Fig. 8 for 1 and 0.5 μm bubble material. The properties for both types of material do change, but these changes are not catastrophic. Also note that the changes in $4\pi M_s$ and W_o are less, on a percentage basis, for the 0.5 μm diameter bubble material. This is a clear advantage as one scales to smaller diameter bubble materials. If one selects the bubble material and subsequent processing conditions carefully, the post-processing values of $4\pi M_s$ and W_o can be identical with the as grown values. Data presented in [2] verify that this is the case for a simple silicon on garnet process, and at this point we will reproduce some of that data. Figure 12(A) shows the relevant structure; $4\pi M_s$ for the as grown bubble film is 695 G. After this structure is laser annealed (after the silicon is recrystallized), $4\pi M_s$ is found to be ~774 G. If the material is next post-laser annealed, in oxygen at 850°C, it is found that the room temperature $4\pi M_s$, after the anneal, will be close to the as grown value (see Fig. 12(B)). Consult [2] and [3] for additional data on the annealing of magnetic bubble films.

SUMMARY

To date, we have demonstrated that it is possible to fabricate semiconductor devices on magnetic bubble substrates. Some problems still exist, but they appear solvable and research on system issues is now merited. Annealing studies indicate the common bubble film compositions are reasonably tolerant of the high temperature processing required to fabricate silicon on garnet devices. The demonstration of silicon magnetodiodes on silicon substrates is particularly important since one can now consider combining bubble detection devices with post-processing electronics on a single substrate.

FUTURE WORK

The next major goal of our research is to fabricate the structure (or those similar to it) shown in Fig. 1 on magnetic bubble substrates, and to use this type of sensor to detect magnetic bubbles. Additional annealing studies, directed at demonstrating and understanding bubble propagation in magnetic films subjected to the silicon on garnet process, will be conducted. Indeed, this future work is very important and necessary if we are to realize a magnetodiode that senses the fringing magnetic field of a magnetic bubble.

REFERENCES

[1]   A. Mohaghegh, S. Cristoloveanu, and J. De Pontcharra, IEEE Transactions on Electron Devices, ED-28, NO. 3, March 1981.

[2]   P.H.L. Rasky, MS. project report, Carnegie-Mellon University, 1984 (unpublished).

[3]   P.H.L Rasky, D.W. Greve, M.H. Kryder and S. Dutta, J. Appl. Phys. 57, 4077, (1985).
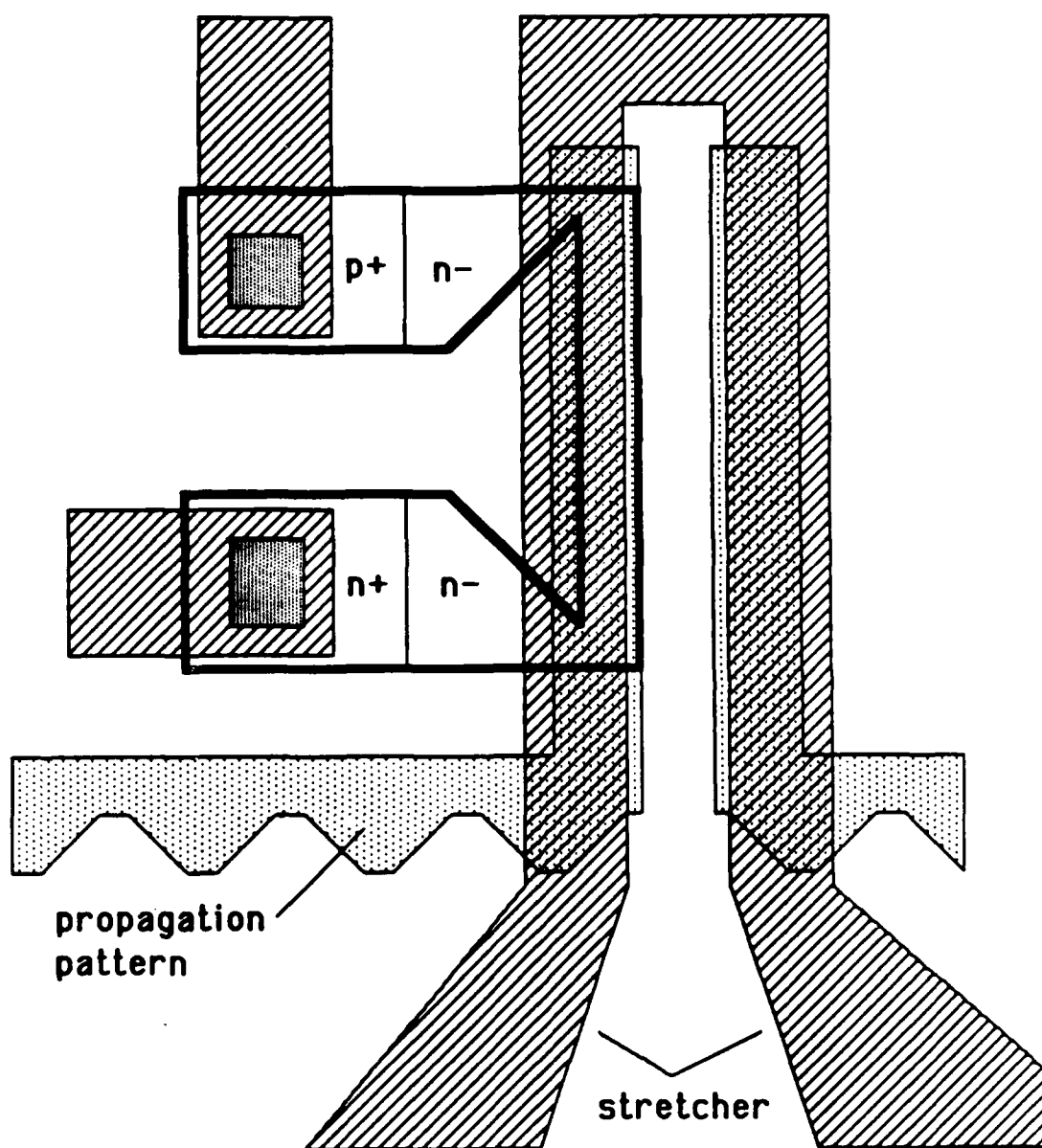
Figure 1:   Silicon magnetodiode integrated with an ion-implanted bubble propagation pattern.
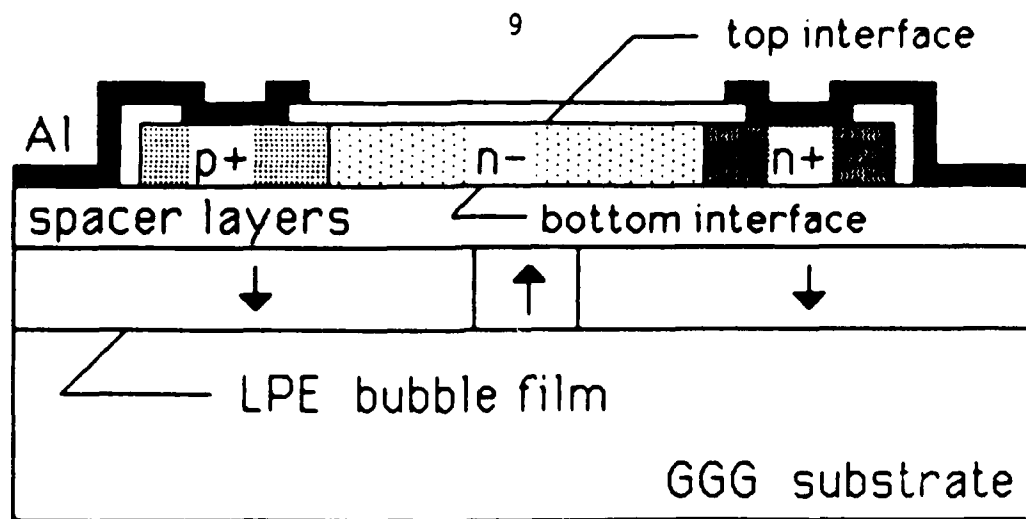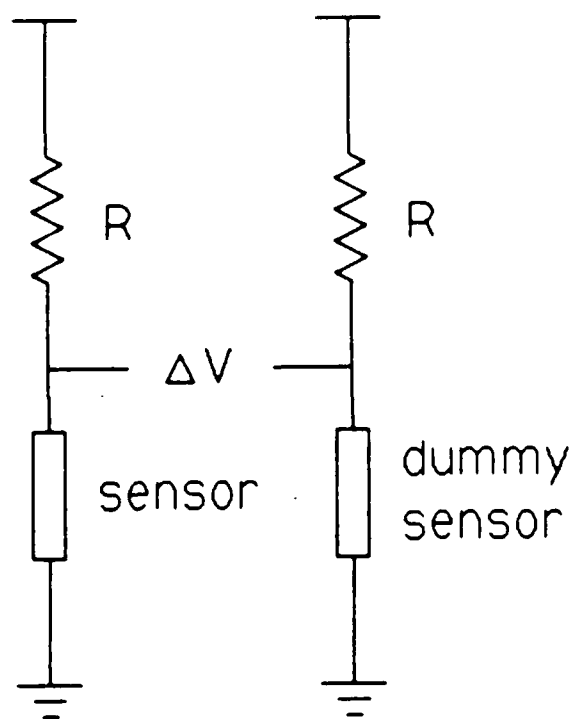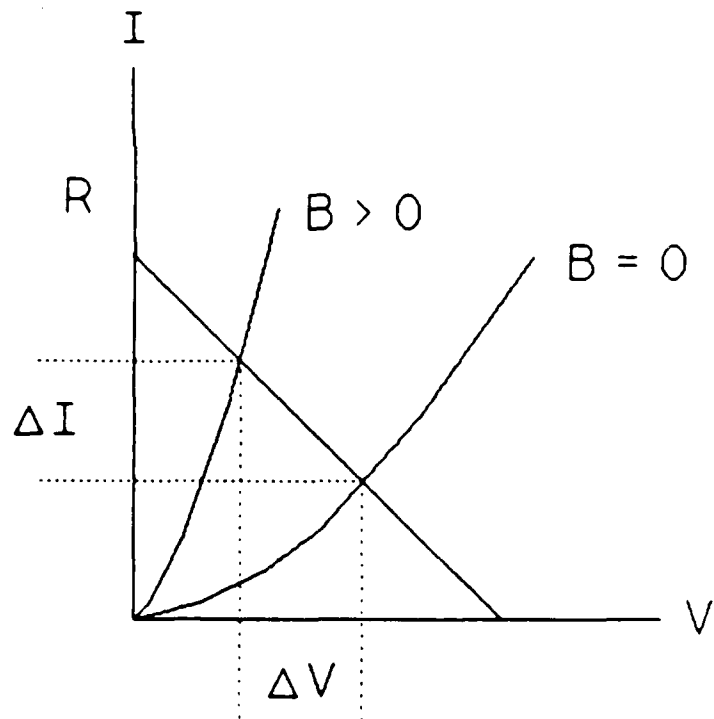
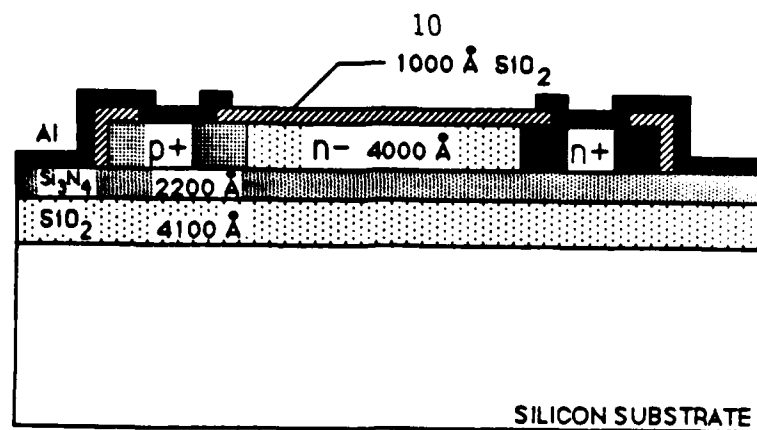Figure 2: Cross section of a silicon on garnet magnetodiode.
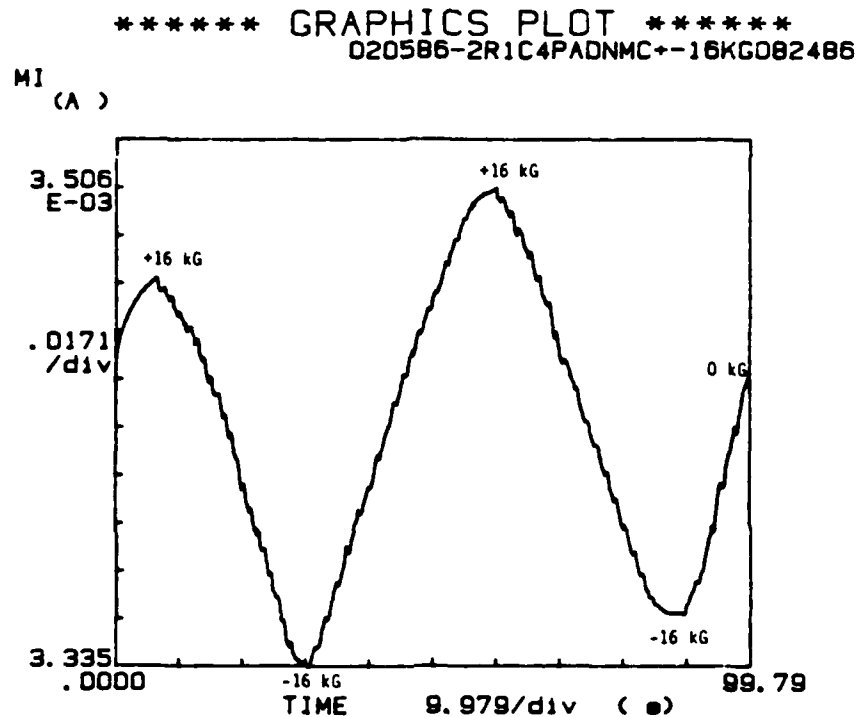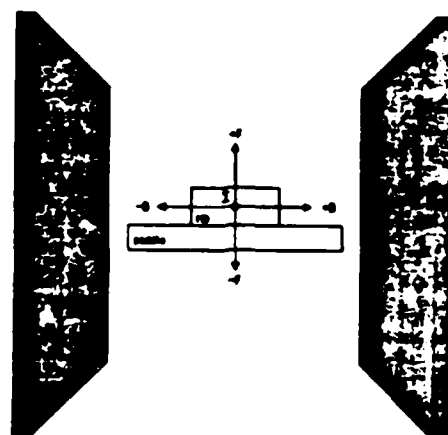

(A)

(B) · ·

Figure 3: (A) Magnetodiode differential detection circuit. $\Delta V = 0$ when no bubble is present (logic 0) and $\Delta V < 0$ or $\Delta V > 0$ when a bubble is present (logic 1). The sensor and dummy sensor have identical structures. Only the senor diode is near enough to the bubble to be affected by its in-plane magnetic field. (B) load line analysis for one half of the circuit shown in (A).

10
1000 Å SiO₂

Al | p+ | n− 4000 Å | n+
Si₃N₄ 2200 Å
SiO₂ 4100 Å

SILICON SUBSTRATE

(A)

****** GRAPHICS PLOT ******
020586-2R1C4PADNMC+-16KG082486

MI (A)

3.506 E-03

+16 kG

+16 kG

.0171 /div

0 kG

(B)

3.335 .0000   -16 kG   -16 kG   99.79
TIME   9.979/div   (s)

(C)

Figure 4:   (A) Cross section of a silicon magnetodiode with a silicon substrate. The diode is 25 μm wide.

(B) Diode forward current I_D with an applied in-plane magnetic field; the field was swept between + and - 16kG.

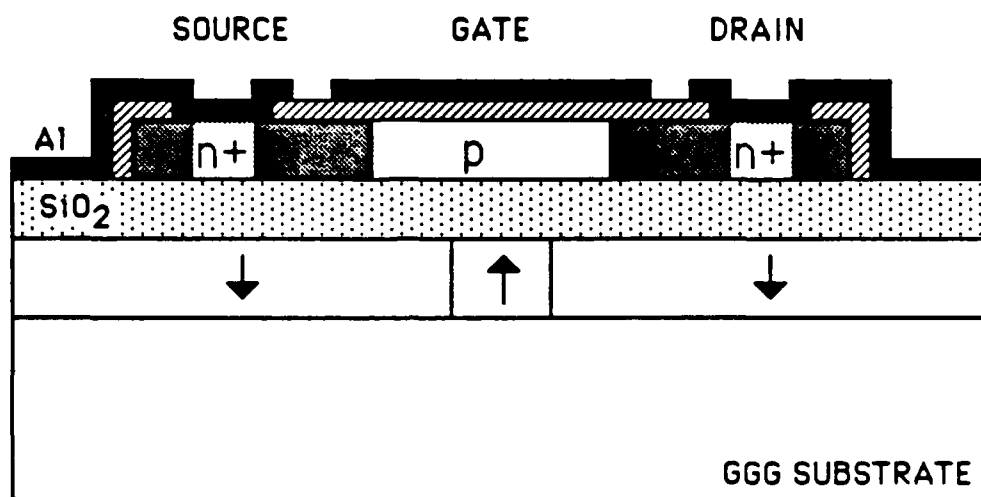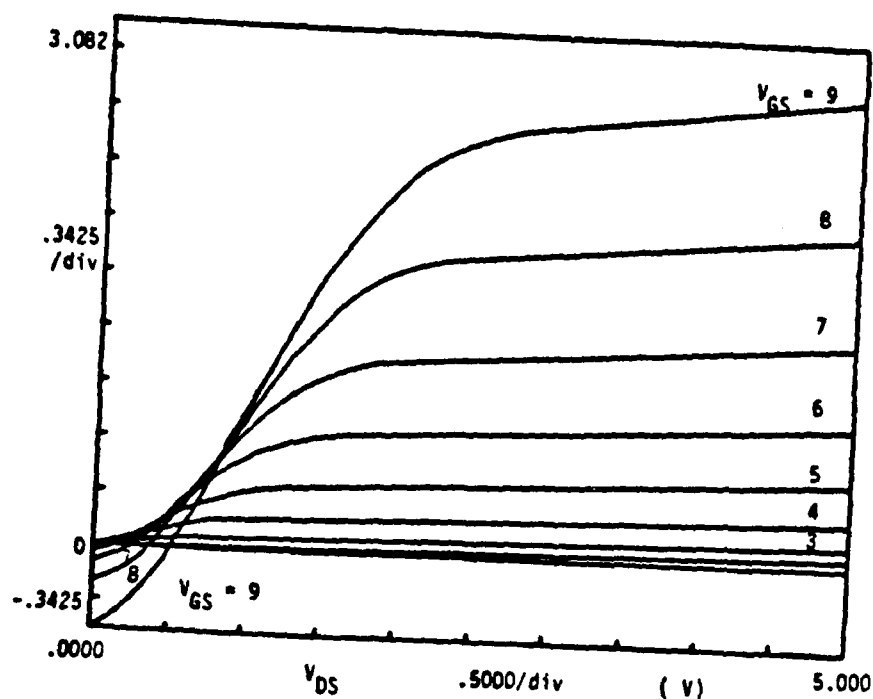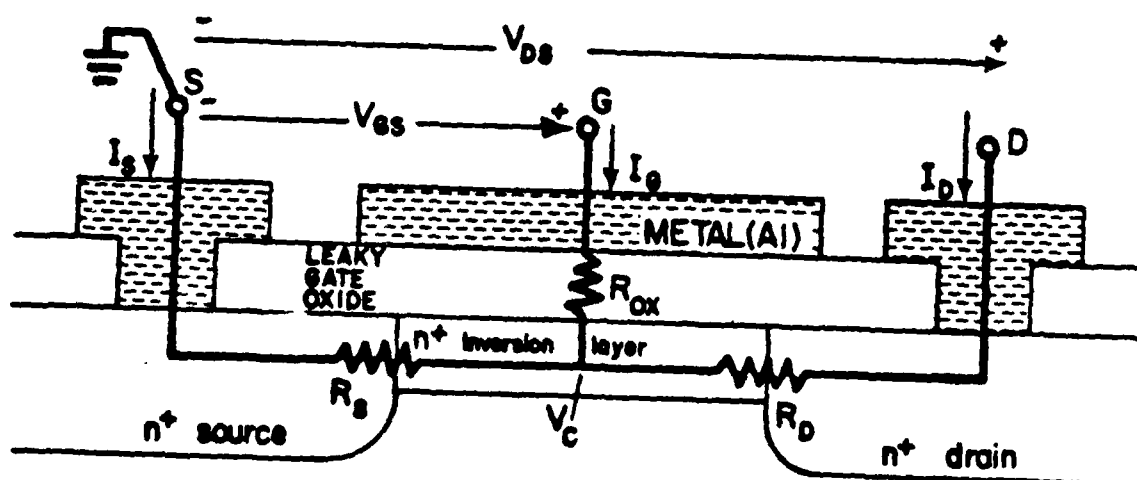(C) Orientation of magnetodiode during measurements.

SOURCE   GATE   DRAIN

Al

SiO2

GGG SUBSTRATE

Figure 5:   Cross section of a silicon on garnet MOSFET with a sputtered oxide
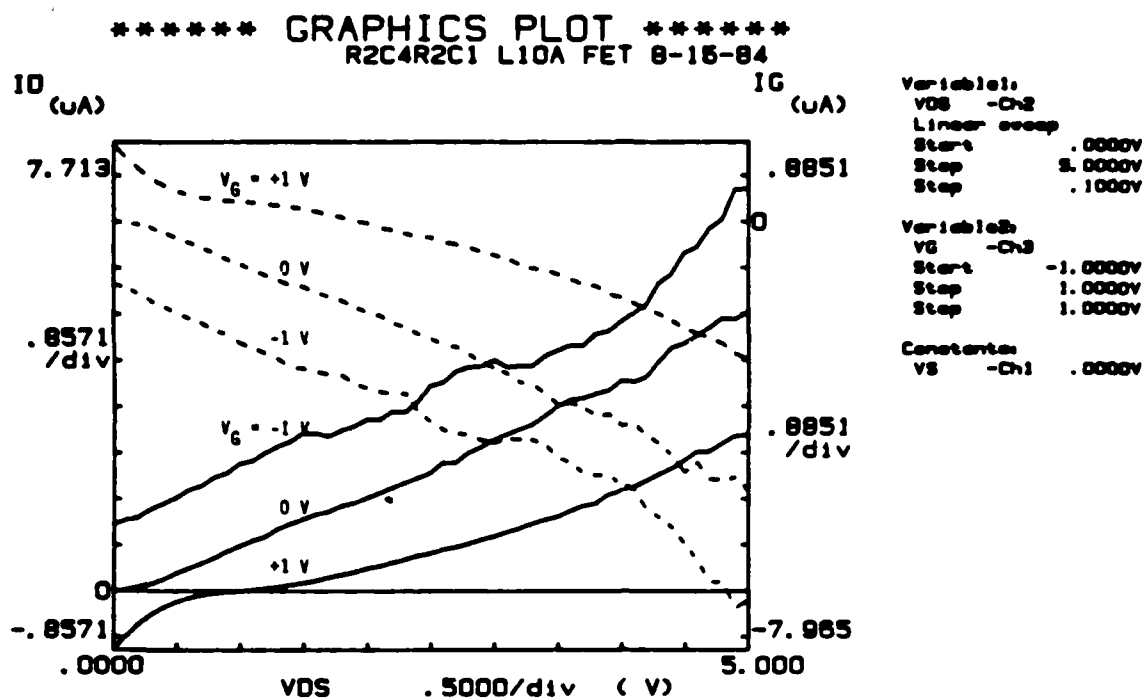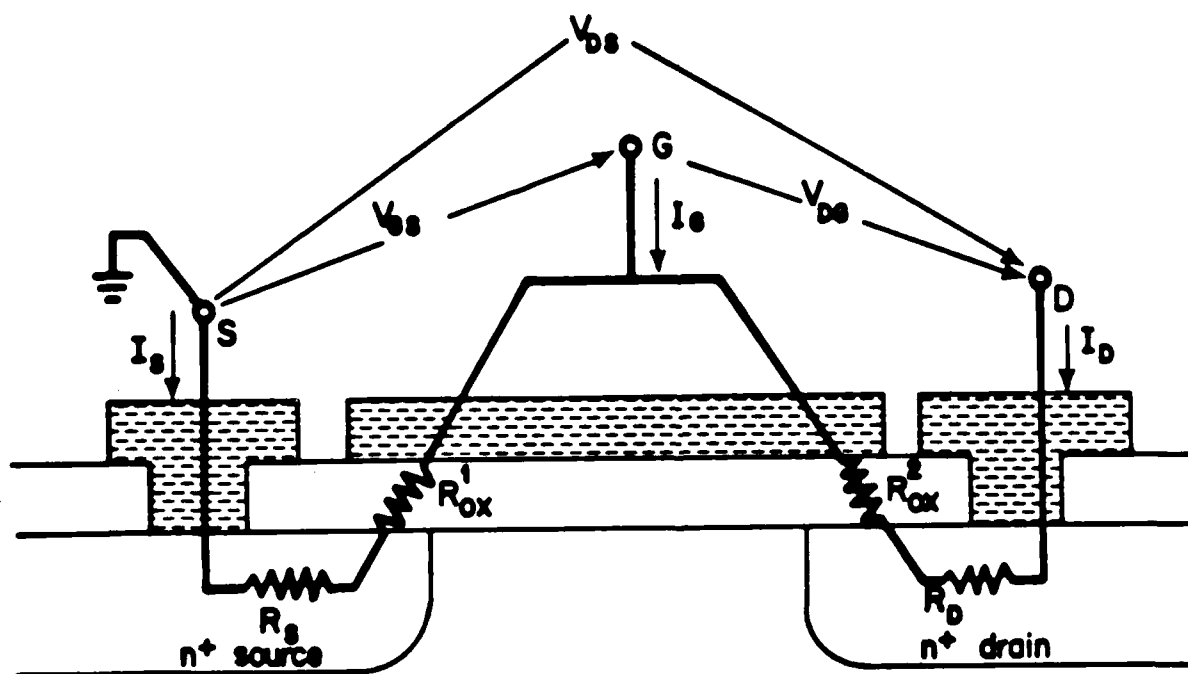   spacer.

Figure 6: (A) Drain characteristics for a silicon on garnet MOSFET adequately modeled by the the circuit shown in part (B) of this figure. The composition of the bubble film is $\{Y_{1.00}Sm_{0.39}Tm_{0.92}Ca_{0.69}\}\{Ge_{0.70}Fe_{4.30}\}O_{12}$. The channel length/width ratio of the MOSFET is $25\mu m/25\mu m$.

(B) Device model for a MOSFET with non-zero, non-catastrophic gate leakage current.

Figure 7: (A) Drain characteristics for a MOSFET adequately modeled by the circuit shown in part (B) of this figure. Dashed curves are plots of I_G vs. V_{DS}. The composition of the bubble film is $(Y_{1.00}Sm_{0.39}Tm_{0.92}Ca_{0.69})\{Ge_{0.70}Fe_{4.30}\}O_{12}$. The channel length/width ratio of the MOSFET is $25\mu m/25\mu m$.

(B) Device model for a MOSFET with non-zero, catastrophic gate leakage current.
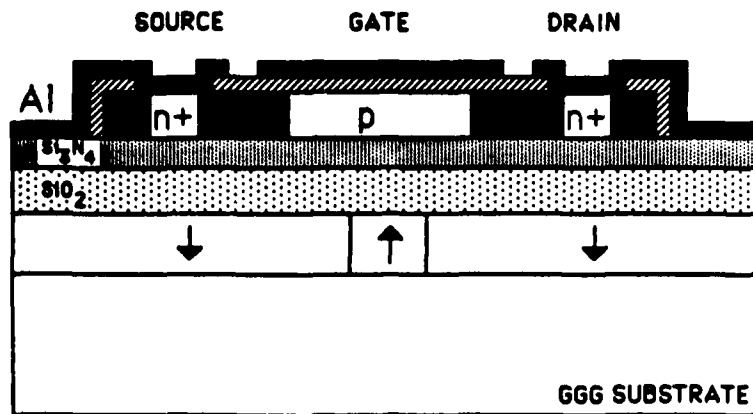
Figure 8: Cross section of a silicon on garnet MOSFET with a double layer spacer.

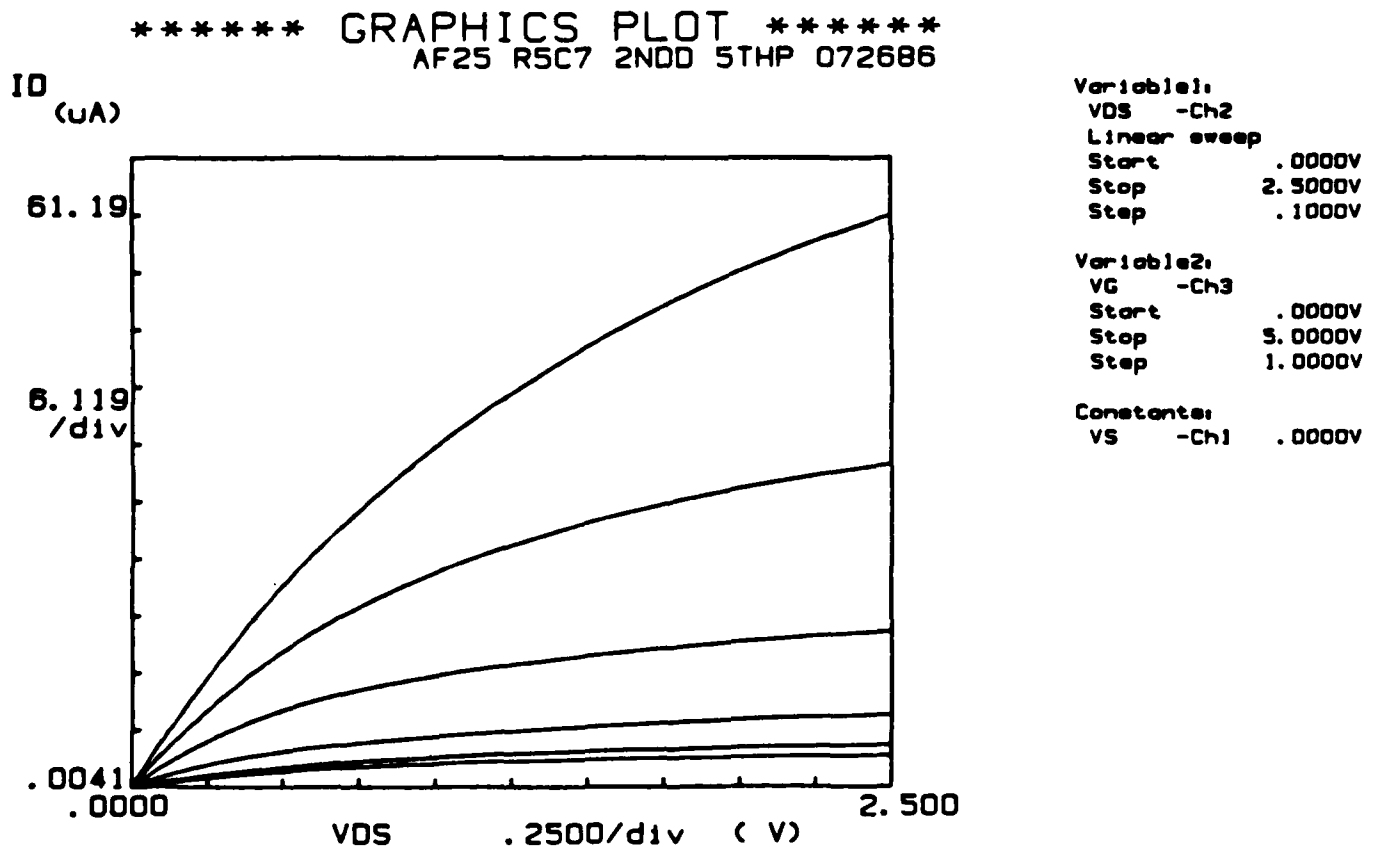

****** GRAPHICS PLOT ******
AF25 R5C7 2NDD 5THP 072686

Figure 9: Drain characteristics for a device with the structure shown in Fig. 8. The SiO_2 spacer layer is 0.41 μm thick and the Si_3N_4 film is 0.85 μm thick. The composition of the magnetic bubble layer is $Sm_xTm_yLu_{3-(x+y)}(Fe_{5-z}Ga_z)O_{12}$. The channel length/width ratio of the MOSFET is 17μm/35μm.

Figure 10: A plot of the gate leakage current I_G vs. the gate voltage V_G with the drain and source at ground potential (V_{DS}=0V). The structure of the device is like that of Fig. 5. A sputtered SiO_2 layer served as the spacer and was $\sim 1\mu m$ thick. The composition of the magnetic bubble layer is $(Sm_{1.2}Lu_{1.7}Tm_{0.1})\{Fe_{5-z}Ga_z\}O_{12}$. The channel length/width ratio of the MOSFET is $12.5\mu m/25\mu m$.
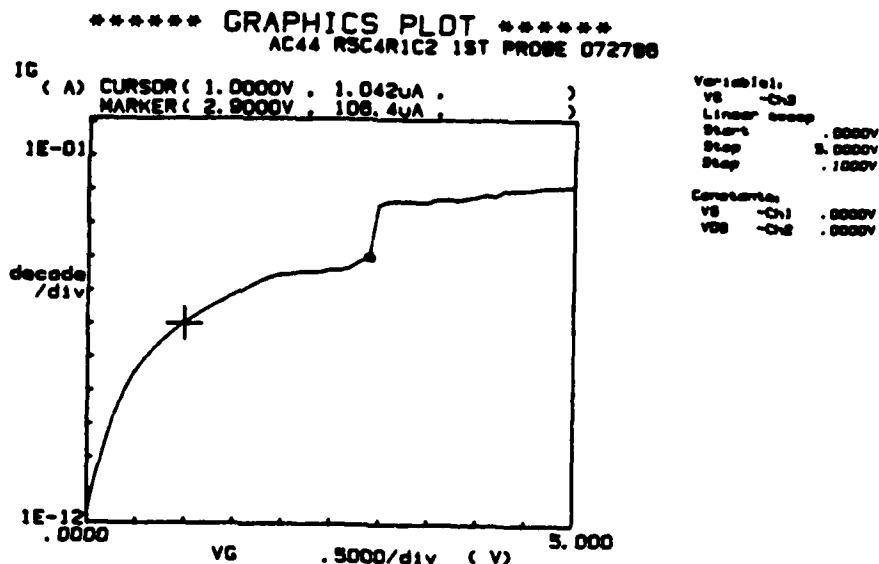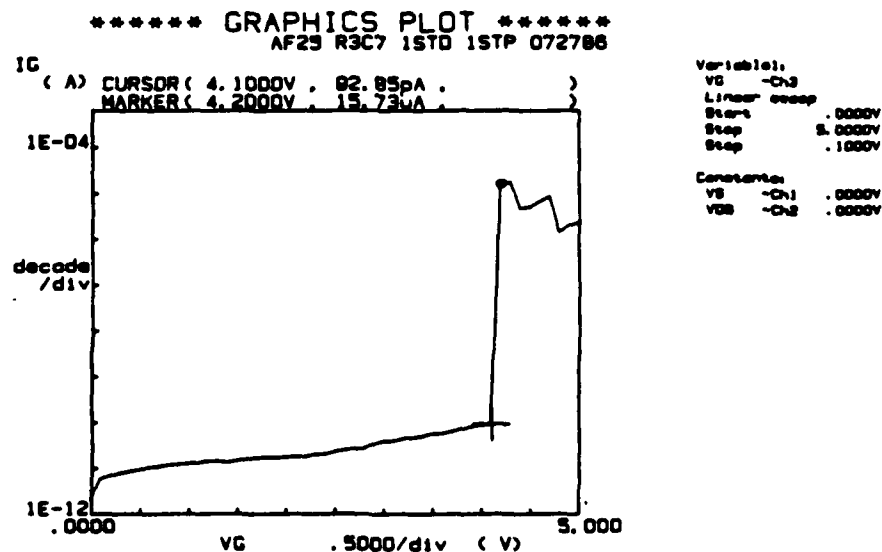

Figure 11: A plot of the gate leakage current I_G vs. the gate voltage V_G with the drain and source at ground potential (V_{DS}=0V). The structure of the device is like that of Fig. 8. The SiO_2 spacer layer is 0.41 μm thick and the Si_3N_4 film is 0.85 μm thick. The composition of the magnetic bubble layer is $Sm_xTm_yLu_{3-(x+y)}(Fe_{5-z}Ga_z)O_{12}$. The channel length/width ratio of the MOSFET is $17\mu m/35\mu m$.
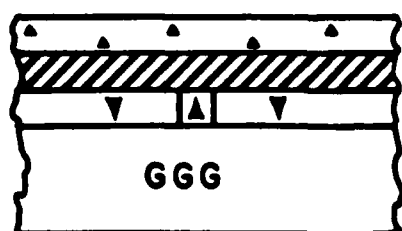
LPCVD Poly-Si ~ 0.75 μm
SPUTTERED SiO₂ ~ 1 μm (Spacer Layer)
BUBBLE LAYER

GGG   **SUBSTRATE**

(A)

LA : o

NLA : - - - -

(B)

$4 \Pi M_s$

TIME (min.)
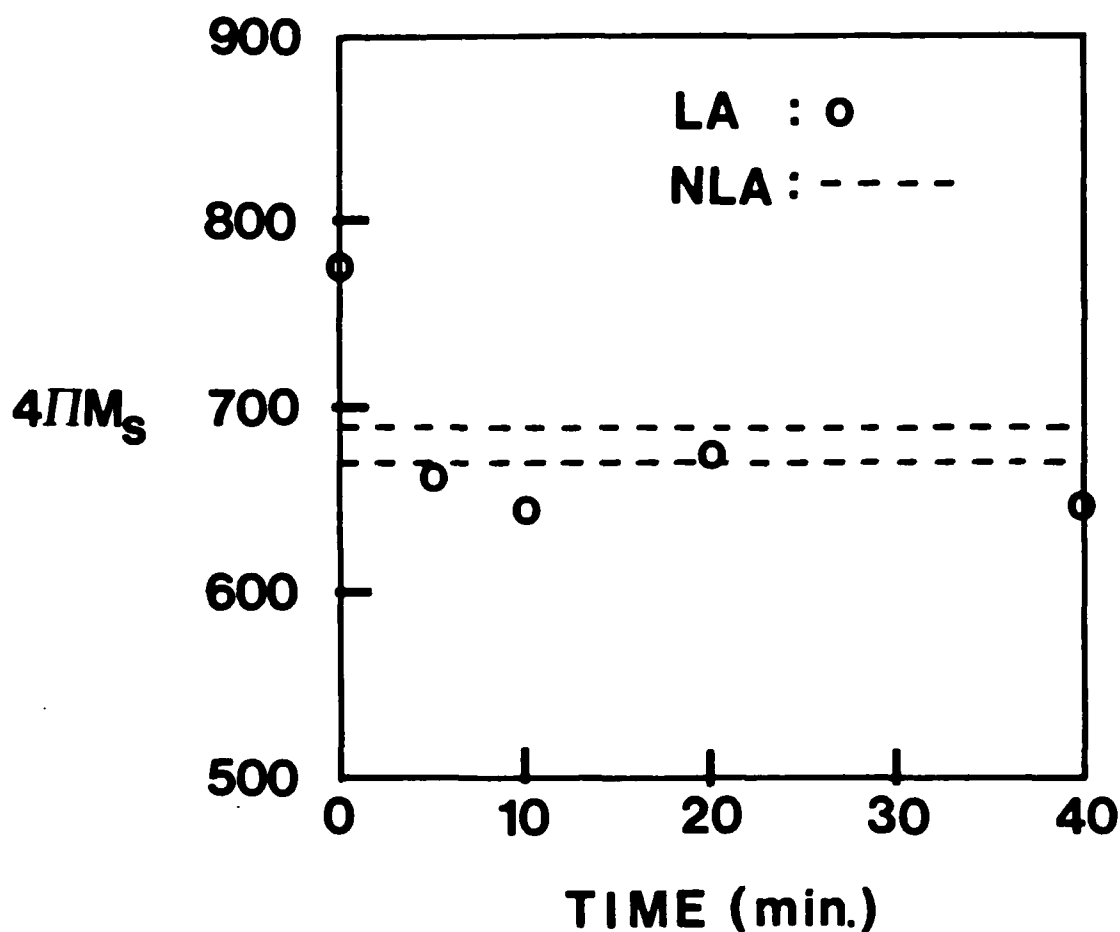
Figure 12:   (A) Silicon on garnet cross section for a simple process.

(B) $4\pi M_s$ after 850°C oxygen post-laser anneals. The post-laser anneals were 5 to 40 min. in length. The data point at 0 min. is for a sample that did not receive a post-laser anneal. The composition of the magnetic bubble layer is $(Sm_{0.3}Gd_{0.4}Tm_{0.73}Y_{1.57})\{Fe_{4.6}Ga_{0.4}\}O_{12}$.

	$4\pi M_s$		$W_o = \frac{P_o}{2}$		
	1 μm	0.5 μm	1 μm	0.5 μm	
As Grown	738	1366	1.43	0.69	23°C
0.41 μm LPCVD SiO$_2$	573	1270	1.79	0.68	64 min. 860°C
0.24 um LPCVD Si$_3$N$_4$	593	1262	1.87	0.67	11 min. 800°C
0.55 um LPCVD Poly-Si	531	1214	1.87	0.64	50 min. 625°C
After Laser Anneal	591	1171	1.15	0.59	350-1412°C

Table 1:   The saturation magnetization $4\pi M_S$ and the zero field strip width W_o at room temperature after typical silicon on garnet process steps. The composition of the magnetic bubble layer is $Sm_x Tm_y Lu_{3-(x+y)}(Fe_{5-z}Ga_z)O_{12}$.

Contiguous Disk Ion Implanted Magnetic Bubble Memory Devices

Soonchul Jo and M.H.Kryder

Introduction

Ion implanted magnetic bubble devices[1] offer an order of magnitude increase in memory density over conventional permalloy devices for a given minimum lithographic feature. This becomes an increasingly important advantage over the permalloy devices as the memory cell size shrinks. In fact, some of the down sized 4 megabit commercial devices are expected to employ ion implanted bubble storage loops (minor loops) instead of permalloy ones and most concerned agree that ion implanted minor loops should be used for the next generation (16 megabit) devices due to the smaller lithographic minimum feature required for the permalloy devices.

In ion implanted devices, chaged walls are utilized to move bubbles along the propagation tracks, which are defined by ion implantation. Figure 1 shows a unit cell of such a track.
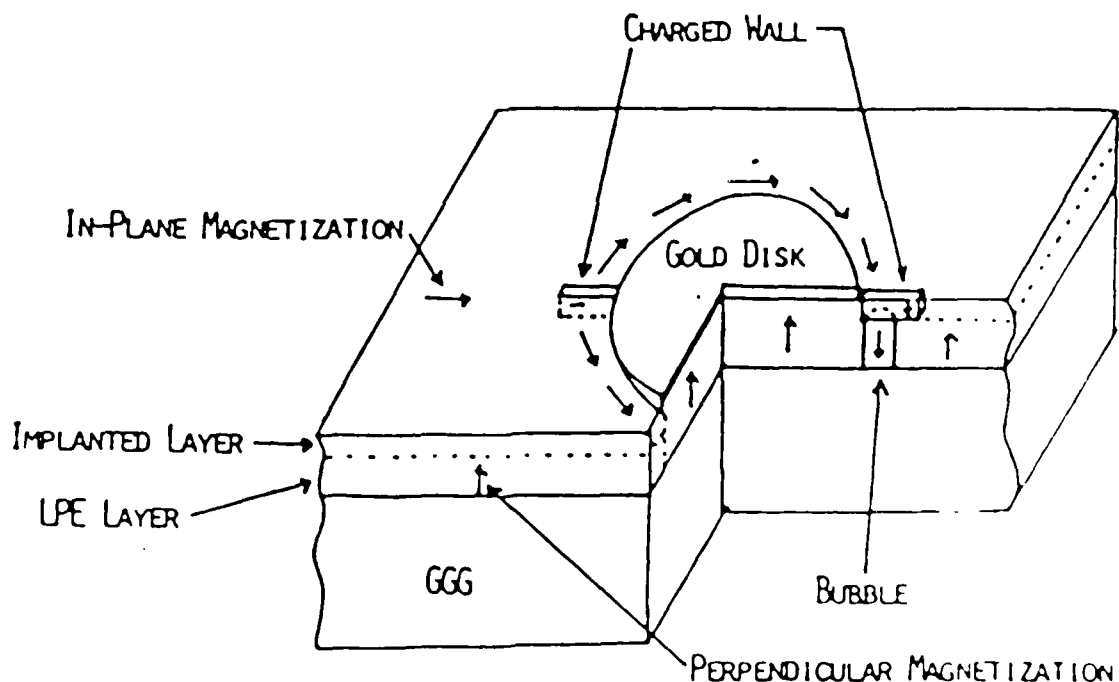
Figure 1: Perspective View of an Ion Implanted Bubble Propagation Cell

Charged walls are formed at the edges of the prapagation tracks and can be moved around by applying a rotating in- plane magnetic field. Bubbles are attracted to the charged walls and follow the movement of them. But this movement of charged walls is not smooth and uniform around the track, instead it shows three fold symmetric behavior, which reflects the three fold symmetry of the garnet crystal. This causes a major difficulty in device design because it results in much worse propagation margins in tracks oriented

in some direction ("bad" track) than others [2,3]("good" or "super" tracks). The mechanisms of the charged wall formation and the three fold symmetric behavior were not well understood until recently Hidaka and Matsutera[4] and, independently Backerra et al.[5] pointed out that partial stress relaxation at the boundary of the unimplated and implanted regions is necessary to form charged walls. Subsequent studies by Kryder and Saunders[6] and, independently Hubert[7] show that partial stress relaxation at the boundary is primarily responsible not only for the formation of the charged walls, but also for the three fold symmetry behavior of the charged walls around the ion implanted patterns. They also pointed out that the three fold symmetry behavior of charged walls can be virtually eliminated by properly choosing magnetostriction coefficients (λ_{100} and λ_{111}) of the magnetic layers. Their theory predicts that if λ_{100} is approximately equall to λ_{111}, the three fold magnetostrictive anisotropy will almost disappear, and bubbles will propagate smoothly along the tracks regardless of their orientations, resulting in isotropic propagation.

The temperature dependence of magnetic bubble propagation is of great practical interest because it essentially determines the operating temperature range of the magnetic bubble memory devices. It has been reported that the operating temperature range of ion implanted devices depends on the garnet film characteristics and the ion implantation conditions. Mizuo and Urai[8] demonstrated that hydrogen implantation allows much higher operating tempeature limits than the helium implantation for the same garnet films. Fratello et al.[9] and Arbaugh and Fairholme[10] showed that bismuth substituted garnet films gave wide operating temperature range

Our objectives of research have been two fold; firstly, design and fabrication of good working ion implanted propagation track devices for 0.5 μm bubbles (which can be used for 16 megabit memory devices) and secondly, experimental investigation of the influence of the three fold magnetostrictive anisotropy due to stress relaxation on device performance using aformentioned propagation track devices During the past year, propagation tracks of various shapes and different orientations for 0.5 μm bubbles were fabricated and tested. Some of the results was published in the September issue of the IEEE Transactions of Magnetics[11] and others will be presented in the upcoming Magnetism and Magnetic materials Conference in Baltimore[12] In this report, we describe an experimental study of propagation of 0.5 μm bubbles in (111) garnets having nearly isotropic magnetostriction. The effects of pattern geometry ion implantation conditions, propagation direction and ambient temperature variation are all considered

Experimental

Propagation tracks with various cell shapes and different orientations were fabricated on 0.5μm bubble garnet films with small $\delta\lambda(=\lambda_{100}-\lambda_{111})$ Garnet films used for the device fabrication are bismuth and dysprosium substituted iron garnets grown by liquid phase epitaxy. The characteristics of one of the films (CA 71) studied are shown in Table 1 The other film (CA 72) studied has slightly different film

characteristics than CA 71, the main difference being somewhat higher effective uniaxial anisotropy (by 250 Oe).

Table 1:   Garnet Film Characteristics (CA 71)

Composition $\{Bi_{0.4}Dy_{0.7}Sm_{0.2}Lu_{1.5}Y_{0.2}\}[FeGa]_5(O)_{12}$

Thickness t $0.65\mu m$

Collapse field H_0 580 Oe

Material length l $0.054\ \mu m$

Magnetization $4\pi M$ 960 G

Uniaxial anisotropy H_k 1850 Oe

Quality factor Q   1.9

Bubble diameter d $0.5\mu m$

Magnetostriction coeff λ_{111} -3.1×10^{-6}

λ_{100} -2.1×10^{-6}

Ion implantation masks for propagation patterns were formed by electroplating gold through a photolithographic mask. Firstly, 80 nm of SiO_2 and the plating base (Mo and Au) were sputtered on the film. Then, photoresist patterns were delineated using 500 nm thick AZ 4070 resist and a Karl Suss contact aligner with a mid U.V. (310 nm) light source. Then, 350 nm of gold was electroplated using Selrex Corporations' BDT 510 gold bath. Current density used was 3 mA/cm^2. After the electroplating, deuterium was doubly implanted to define the prapagation tracks. Implantation energies and dosages were varied to find optimum conditions for bubble propagation. Implantation energies and dosages which give approximately 230 nm of implatation depth and relatively uniform implant with in plane Q of -2.5 gave good propagation margins for most of the 2.5 μm period patterns. The ion implantation conditions are listed in Table 2

Table 2:   Ion Implatation Conditions

	Ion species	Energy	Dosage
1st implantation	Deuterium	46 Kev	$7.5\times10^{15}/cm^2$
2nd implantation	Deuterium	26 Kev	$5\times10^{15}/cm^2$

Finally, the gold implantation masks together with the plating base were stripped with Au etchant and aluminum was evaporated to be used as the reflection layer for the observation of bubbles by a polarized light microscope. High Faraday rotation due to Bi substition in the garnet film and the Al mirror gave excellent visibility so that bubbles were easily observed up to collapse.

The devices were tested by measuring quasi-static (1 Hz) bias margins for "good" and "bad" tracks. Data patterns were randomly generated by slowly raising the bias field from the bubble stripe out state. Propagation around the corners was included in the bias margin measurements and the number of cycles of propagation varied from a few tens to 250. The propagation pattern shapes studied in this paper are illustrated in Figure 1.

Temperature variation of the propagation tracks was achieved by changing the ambient temperature of the device. The device chip was placed at the center of a double donut shaped bias magnet and the magnet was sealed. Then, temperature controlled air or dry nitrogen was blown in to maintain the desired temperature. The temperature was monitored by a thermocouple placed near the device. Enough time was allowed for the chip to reach a temperature equilibrium before any measurement was made. The accuracy of the temperature controller was ± 1 °C throughout the temperature range tested.
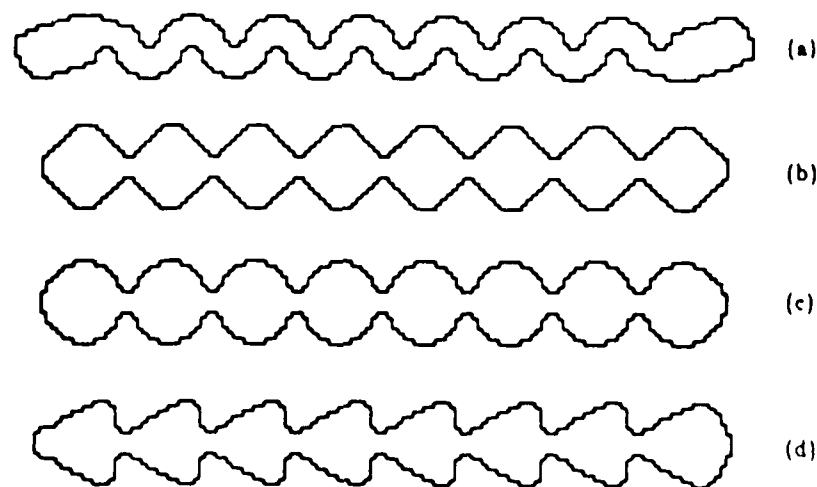

Figure 2: Bubble Propagation Shapes
(a) Snake (b) Diamond (c) Circle (d) Triangle

Results and Discussion

Quasi-static bias margins of "good" and "bad" 2.5 μm period tracks for diamond, circle, triangle and snake shaped bubble propagation patterns were measured. Figures 3,4 and 5 show results obtained from film CA71. "Good" and "bad" track margins for diamond shaped patterns are shown in Figure 3, which show almost identical bias margins for "good" and "bad" tracks with the minimum in plane drive field of 30 Oe and the margin width of 80 Oe (15% of the mid bias). This is a dramatic improvement of "bad" track margins over those typically seen in ion implanted devices with conventional garnet films.

Bias margins for other cell shapes show slightly higher minimum drive fields for "bad" tracks, but similar margin widths for both tracks except the snake shape. Overlapping bias margins of "good" and
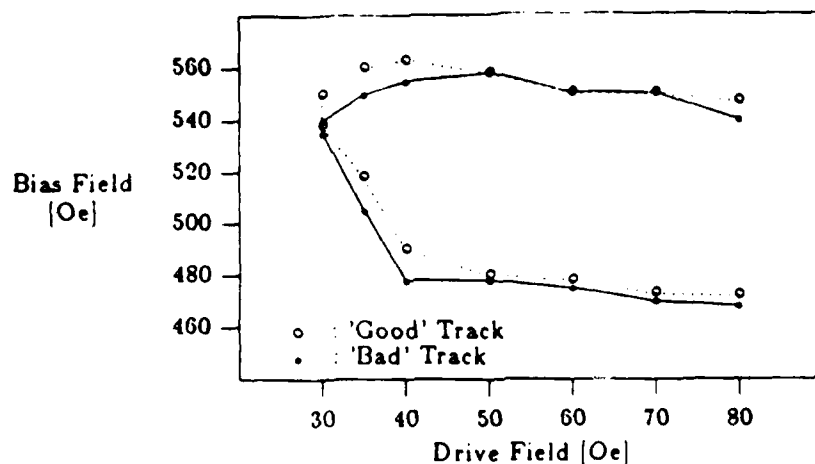
Figure 3: Margins for 2.5 μm period Diamond Shaped propagation pattern
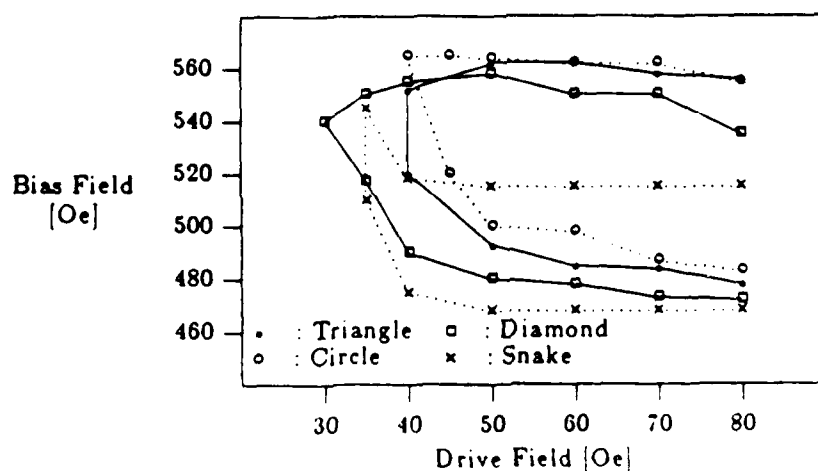Film CA 71

Figure 4: Overlapping Margins for 2 5 μm Period Diamond.
Triangle, Circle and Snake Patterns Film CA71

"bad" tracks for diamond, triangle. circle and snake shaped propagation tracks are shown in Figure 4
The best overlapping margins are obtained from the diamond shape and the worst from the snake. The
reason that the snake patterns have the worst overlapping bias margins is mainly due to the skidding of
bubbles along the bad tracks (propagation of more than one period of the track during one cycle of the
in-plane drive field) at high bias fields. On the other hand, the snake patterns show the best "good" track
margin (25 Oe minimum drive and 15% margin width). The "good" and "bad" track bias margins for
snake patterns are plotted in Figure 5

Figures 6 and 7 illustrate bias margin measurements obtained from snake patterns on film CA 72 CA
72 has slightly different film characteristics than CA71, the main difference being somewhat higher
effective uniaxial anisotropy (by 250 Oe). Ion implantation conditions were the same as CA 71, which
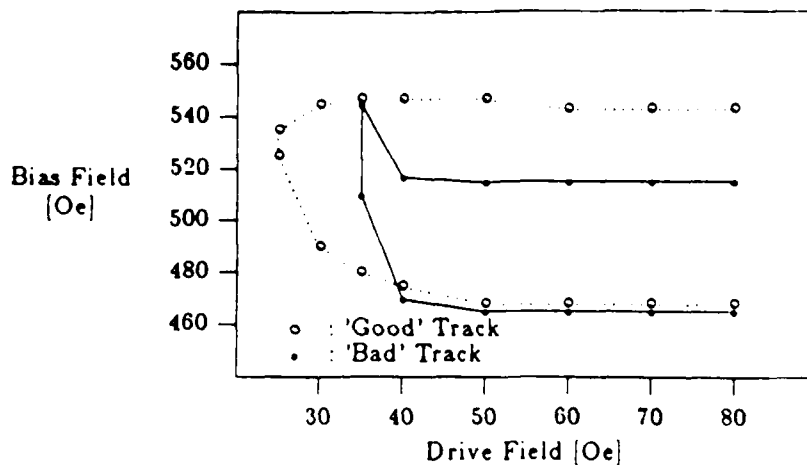
**Figure 5:** Margins for 2.5 μm Period Snake Shaped Patterns
Film CA71

were shown in Table 1. "Good" and "bad" track margins for 2 μm period snake patterns are shown in Fig. 6. Figure 6 (a) shows the results obtained from the patterns with the cusp depth to track period ratio of 0.44, while Figure 6 (b) shows margins from the patterns with the cusp depth to track period ratio of 0.38. It is clear from the margin plots that a slight change of cusp dimension(1/8 μm) could significantly affect the bias margins, especially for the "bad" tracks. It seems from these plots and previous margin plots of film CA 71 that sharper cusp definition (for example, snake patterns with deeper cusps and diamond patterns) help prevent bubbles from skidding along "bad" tracks. As Lin et al.[1] pointed out, wider and smoother cusps yield better margins as demonstrated in "good" snake patterns. But, at the same time such cusps seem to promote the skidding failure mode in "bad" tracks.

Figure 7 shows bias margins for 2 5 μm period snake patterns made with film CA 72 They have the same cusp shape as the patterns whose margins are shown in Figure 5(CA 71). CA 71 and CA 72 were ion implanted with the same conditions and at the same time as noted earlier. The main difference in the films was that CA 72 had somewhat higher effective anisotropy than CA 72(by 250 Oe) Thus, this resulted in a slightly lower (magnitude) in-plane Q for CA 72 than CA 71 The "bad" track margin shows considerable improvement in margin width compared with CA71, even though the minimum drive field of the good track margin has increased slightly (by 5 Oe) Still, the overlapping bias margin is significantly better than the margin of CA71 which exibits a minimum drive of 35 Oe and margin width of 70 Oe (14% of mid bias value)

The failure mechanism of the "bad" tracks in the snake pattern at high bias fields was bubble collapse at low and medium drive and bubble skidding at high drive. This contrasts to the predominant skidding failure mechanism of film CA 71 This shows that with proper ion implantation, we can largely avoid skidding failures at high bias, producing good "bad" track propagation. It is to be noted that the
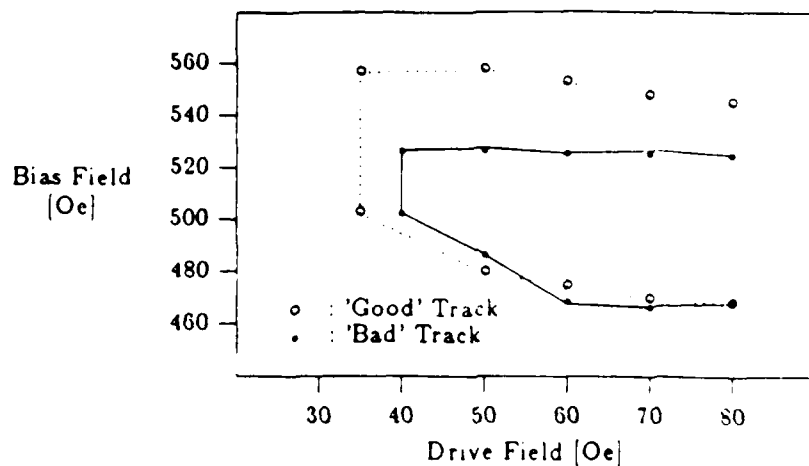
(a)
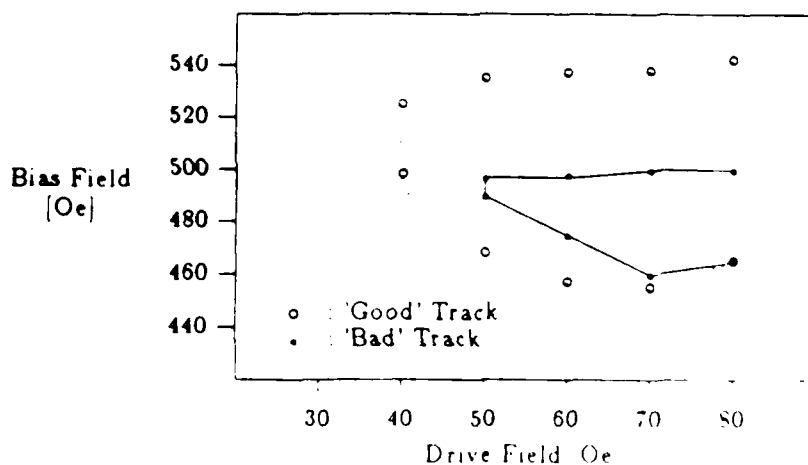
(b)

Figure 6: Margins for 2 μm Period Snake Patterns with
(a) Cusp to Period Ratio of 0.44 (b) Cusp to Period Ratio of 0.38
Film CA 72

skidding failure mode is not limited to snake patterns. It was observed in other propagation patterns with different ion implantation conditions.

"Good" and "bad" track bias margins of diamond and circular propagation patterns of sample CA 72 were measured from 0 °C to 130 °C. Figure 8 shows the temperature dependence of the minimum drive fields of diamond and circular propagation patterns as a function of temperature. The curves show a monotonic decrease of the minimum drive as the temperature is increased. The decrease of the minimum drive was previously attributed to the decrease of the cubic magnetocrystalline anisotropy[8]. Since it is
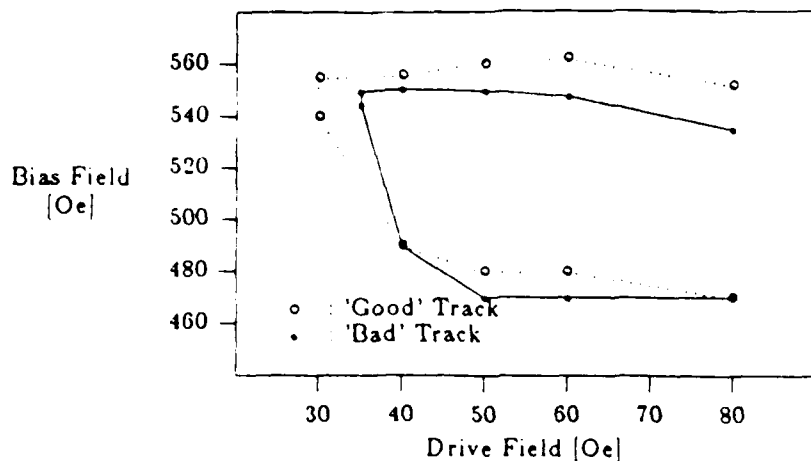
Figure 7: Margins for 2.5 μm Period Snake Patterns
Film CA 72

now believed that the dominant source of the three fold anisotropy is the magnetostrictive anisotropy due to partial relaxation of the stress at the boundary of the implanted and unimplanted regions[6,7], it seems to be more reasonable to assume that the decrease of the minimum drive is mainly due to the decrease of the magnetostriction coefficients and the difference of the two coefficients λ_{111} and λ_{100} which is proportional to the anisotropy energy[6]. The temperature dependence of magnetostriction coefficients of $Sm_3Fe_5O_{12}$ and $Dy_3Fe_5O_{12}$ as well as the difference of the two coefficients shows a steady decrease as the temperature increases[13]. Since the magnetostriction coefficients of our garnet film are mainly determined by Dy and Sm, the above explanation seems to be reasonable. Diamond patterns showed lower drive fields for both "good" and "bad" tracks (less than 40 Oe). It is interesting to see that the minimum drive fields for supposedly "bad" tracks are actually lower than "good" tracks for most of the temperature range. This will be explained later on.

Figure 9 shows bubble propagation bias margins at 60 Oe drive field as a function of chip temperature of diamond and circular patterns. The margins shifted downward monotonically as the temperature increased with a coefficient of roughly -0.27%/°C (at 50 °C). Diamond patterns showed the wider overlapping margin of "good" and "bad" tracks (80 Oe or 15% of mid bias value at 40 °C). Circular patterns showed almost no margin width variation throughout the temperature range tested. At 130 °C they still showed 55 Oe (14% of mid bias) of overlapping bias margin. Margin degradation at high temperature was due to a decrease of collapse field at high drive field.

It is interesting to note that the collapse field of the "bad" tracks in most of the temperature range is actually slightly higher than that of "good" tracks. The reason why the collapse field of "bad" tracks is higher than that of "good" tracks is as follows. To understand the problem, we observed the charged wall (and bubble) direction as a function of drive field around an unimplanted disk of diameter 4 μm at
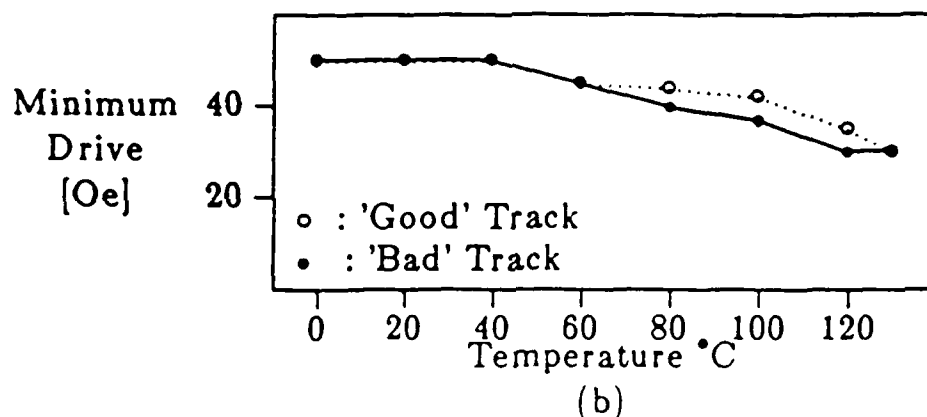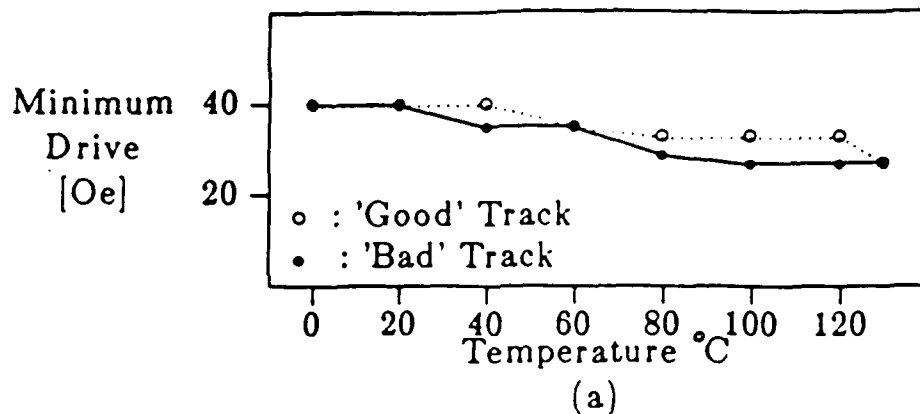
Figure 8: Temperature dependence of minimum drive field for (a) diamond
and (b) circular patterns

low drive field (15 Oe). The crystal orientation of the disk and bubble jumping directions due to charged

wall flip motion[14] are shown in Figure 10 (a) The $\overline{1\,1\,2}$ direction is designated as $0°$ of rotation. As is

shown in the figure, charged wall (and bubble) jumping occurs at $20°$, $180°$ and $290°$ Figure 10 (b) shows

propagation tracks oriented in the "good" direction($\overline{1\,1\,2}$) and "super" and "bad" direction

(perpendicular to "good" direction). Short lines around the tracks indicate in-plane drive field directions

where the charged wall flip motion or the bubble jumping occurs. It is to be noted at this point that the

most difficult part of the propagation process is to move the bubbles out of the cusps. Suppose that the

drive field rotates in a clockwise direction. Bubbles leaving cusps from the bottom side of the "good"

tracks are subject to charged wall jumping as they start to move out of the cusps while bubbles on the

top side of the tracks do not encounter such adverse conditions as they leave the cusps. Therefore, the

failure mode at high bias is bubble collapse at the bottom cusps.

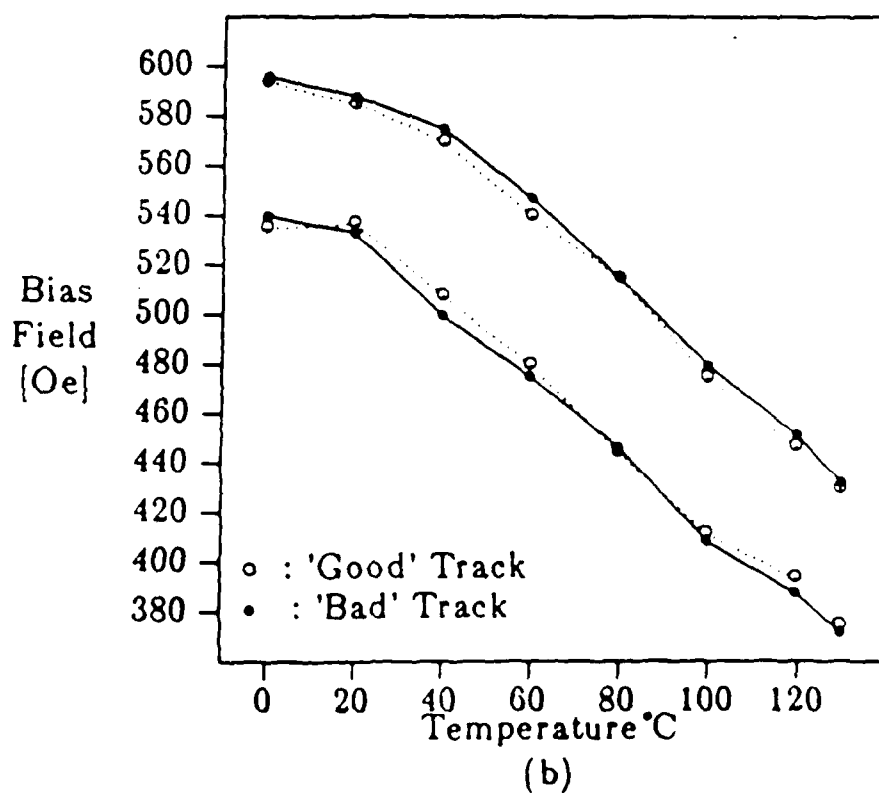Now consider the "bad" track. Here, bubbles are subject to charged wall jumping after they come out

(a)

(b)
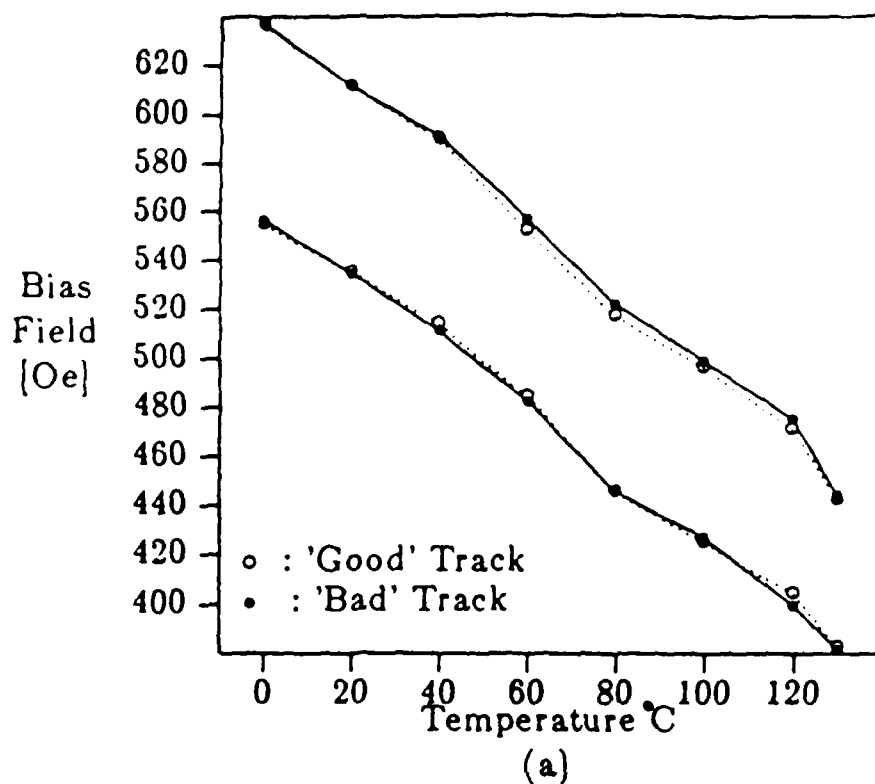
Figure 9: Temperature dependence of bias margin at 60 Oe of drive field for (a) diamond and (b) circular patterns

28

(a)

(b)
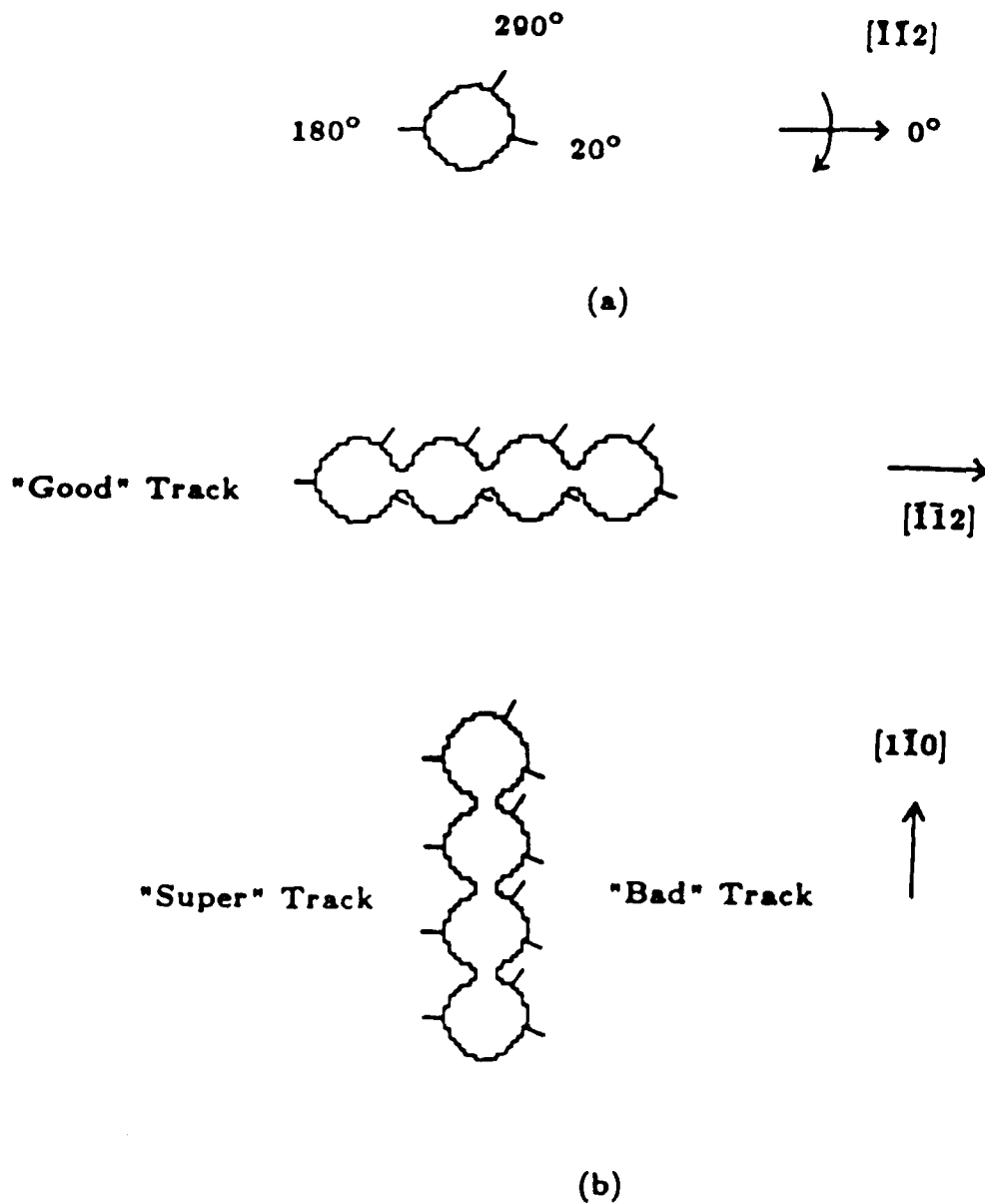
Figure 10: Charged wall flip (and bubble jumping) directions of (a) unimplanted
disk and (b) propagation tracks

of the cusps. Therefore bubbles can follow the jumping motion of the charged wall relatively well and thus have higher collapse field. This charged wall behavior difference is believed to be responsible for the slightly higher collapse field of "bad" tracks than "good" tracks. It is to be remembered that the garnet film is nearly isotropic to begin with

Futher evidence to support this explanation is found by reversing the in-plane field rotation direction

Now bubbles both on the top side of the "good" track and on the "bad" track encounter charged wall jumping after they get out of the cusps. Therefore, we expect that the bubbles on both tracks will behave similarly. It is to be noted that all the margin plots presented so far were measured using clockwise rotating in-plane fields. Figure 11 shows bias margins of diamond patterns obtained by clockwise (a) and counterclockwise (b) rotating in-plane fields. Figure 11 (b) shows an increase of "good" track collapse field and almost identical bias margins for both "good" and "bad" tracks. This is in agreement with our explanation above.

As was mentioned earlier, the minimum drive field of "bad" tracks are generally lower than that of "good" tracks. By looking at Figures 8 and 9, we find excellent correlation between the minimum drive field and the collapse field of respective "good" and "bad" tracks. When the collapse field of the "bad" track is higher than that of the "good" track, the minimum drive of the "bad" track is lower than that of the "good" track and vice versa. This is easily explained by the previous argument. When the collapse field is higher, it is easier for the bubbles to come out of the cusps, therefore the minimum drive is lower and vice versa.

Conclusions

Bubble propagation tracks of various cell shapes were fabricated on bismuth substituted 0.5 μm garnet films with small magnetostriction coefficient difference. Bias margin measurements show great improvement of "bad" track margins for all cell shapes tested. Diamond shaped patterns exibited the best overlapping bias margins. Although snake shaped patterns show the best "good" track margins, their "bad" track margins are most suceptible to a skidding failure mechanism at high bias fields, which could significantly degrade the margins. It was found that "bad" track margins (notably of snake patterns) are very sentitive to ion implantation conditions and pattern cusp shape. Nearly isotropic bubble propagation was achieved for all the track shapes tested by careful adjustment of ion implantation conditions and track cusp shape. The temperature dependence was measured over the temperature range of 0 °C to 130 °C. The results show good overlapping bias margins of "good" and "bad" tracks up to 120 °C (at least 13% of mid bias). The wider overlapping margin width (at least 14% of mid bias) and the lower minimum drive field (at most 40 Oe) over the temperature range tested were obtained from the diamond patterns. Circular patterns showed a consistent margin width (60 Oe) throughout the temperature range The patterns exibited slightly higher collapse fields for "bad" tracks than "good" tracks depending on the rotation sense of the drive field This is explained by the fact that the charged wall flip motion occured when the bubble was being pulled out of a cusp for the "good" tracks, but after coming out of a cusp for the "bad" tracks.
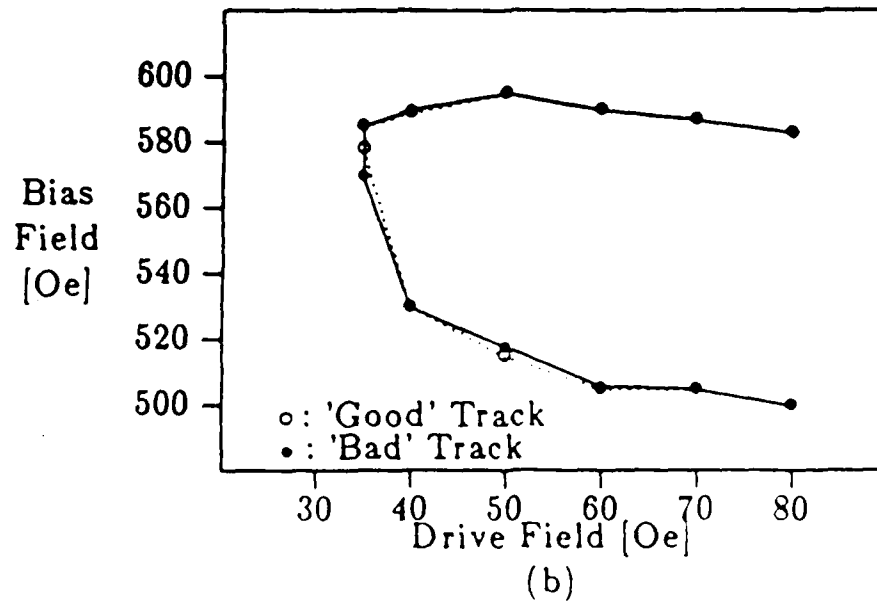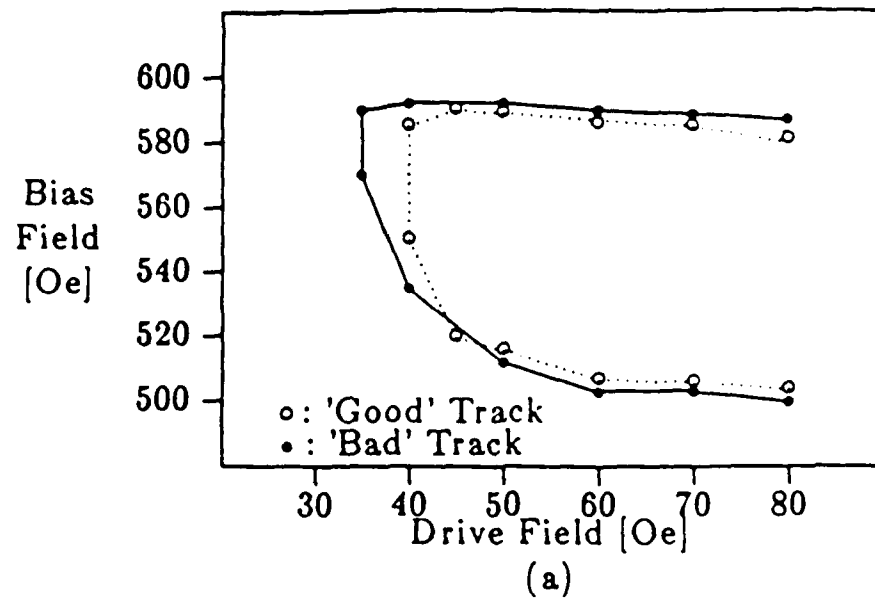
Figure 11: Bias margins of diamond patterns with (a) clockwise and (b) counterclockwise rotating drive field at 40 °C

Future work

More propagation track devices will be fabricated on garnet films with various combinations of magnetostriction coefficients(λ_{111} and λ_{100}). By testing these devices, charged wall formation and bubble propagation mechanisms will be studied and related to the three fold magnetostrictive anisotropy

References

1. Y.S. Lin, G.S. Almasi and G.E. Keefe, IEEE Tran. Mag., MAG-13, No.6, 1744(1977).

2. Y.S. Lin, G.S. Almasi, D.B. Dove, G.E. Keefe and C.C. Shir, J. Appl. Phys , 50(3), 2258(1979)

3. R. Wolfe and T. J. Nelson, IEEE Tran. Mag., MAG-15, No.5,1323 (1979).

4. Y. Hidaka and H. Matsutera, Applied Physics Letters, 39 No.1, 116 (1982).

5. S.C.M. Backerra, W. H. De Roode and U. Enz, Phillips J. Res., 36.112 (1980).

6. M.H. Kryder and D.A. Saunders, IEEE Tran. Mag.,MAG-19, No.5, 1817(1983).

7. A. Hubert, J. Magnetism and Magnetic Materials, 31-34, 976(1983).

8. K. Mizuno and H. Urai, IEEE tran. Mag.,MAG-21, No.5, 1706(1985)

9. V.J. Fratello, R.D. Pierce and C.D. Brandle, J. Appl. Phys., 57(8), 4043(1985).

10 L.G. Arbaugh Jr. and R.J. Fairholme, IEEE tran. Mag., MAG-22, No.5, 1287(1986)

11. S Jo and M H. Kryder, IEEE tran. MAG., MAG-22, No.5, 1278(1986)

12 S Jo and M.H Kryder, To be presented at the Magnetism and Magnetic Materials Conference in

Baltimore

13. G. Winkler, *Magnetic Garnets*, Friedr. Vieweg & Sohn, 1981

14. Y.S. Lin, D.B. Dove, S Schwarzl and C C Shir, IEEE Tran. MAG., MAG-14, No.5, 494(1978)

LPE GROWTH OF MAGNETIC BUBBLE GARNETS.

M. Ramesh, R. O. Campbell and M. H. Kryder.
Department of Electrical and Computer Engineering.
Carnegie Mellon University, Pittsburgh, Pa 15213.

Section I Introduction

The main thrust of our LPE garnet film growth program is to develop> films suitable for fabrication of high density, high performance magnetic bubble devices. In order to achieve the desired high storage densities, it is necessary to go for films which can support sub-micron diameter bubbles. We have been able to develop several such materials that are useful for device work. In particular, we focus our efforts in developing 0.5 μm diameter bubble films, which have ideal material properties.

Most bubble devices fabricated on the films developed in our facility use Ion-Implanted Contiguous Disk patterns on garnets. This has hitherto been complicated by the anisotropy in propagation margins in these films. Devices fabricated on a [111] garnet film[1,2], for example, have been shown to exhibit a three-fold symmetry for bubble propagation. Those tracks parallel to [11$\overline{2}$] direction were found to have acceptible margins(Referred to as 'good tracks'), whereas for tracks oriented perpendicular to [11$\overline{2}$], very large propagation margins were observed for one side('super tracks') with anamolously small margins on the other side('bad tracks'). Although, initially this three-fold anisotropy was attributed to magnetocrystalline anisotropy, later analysis revealed that these effects are primarily caused by stress-induced anisotropy[3]. This led Kryder and Saunders[4] to propose that these anisotropic effects could be eliminated by growing garnet films with negative, equal magnetostriction coefficients. $\lambda_{111} = \lambda_{100}$ This is an additional requirement in the development of new high quality bubble materials

A computer program was developed as a part of the materials research. to model various film compositions from a given set of user-defined needs and to estimate their physical properties This greatly eased the film design and provided new film compositions, especially for sub-micron bubble diameter films and isotropic magnetostriction films The computer program has a database of several Rare Earth and Transition Metal elements and the current models to estimate various parameters such as uniaxial anisotropy energy Films grown using the

computer-aided design technique have been reasonably close to estimated design parameters and have been convenient starting points for eventual fine-tuning. The computer program has also been used to make several other garnet films for other purposes.

The LPE film growth furnace itself has been updated and modernized periodically with the ultimate aim of automating the whole growth operation using microprocessors for better and more uniform films.

This part of the report discusses the computer aided film/melt design, which is the starting point for all our bubble materials research, in Section II. Film growth technique is then described in Section III. This is followed by a section on Film Characterization (Section IV). Section V is on the bubble materials developed in our facility with an emphasis on the 0.5 μm, isotropic magnetostriction materials. Magnetic bubble devices need to perform well over a wide ambient temperature range and some preliminary results of our temperature studies are presented in Section VI. Section VII concludes this discussion with a brief mention of work that is currently in progress. with a look at the projects to be undertaken in future.

Section II Computer Aided Film/Melt Design Program

The computer aided film design system has been developed to quickly produce film compositions that will satisfy many criteria concurrently. By using the properties of the film constituents such as rare-earths, iron and iron dilutants, the program can extrapolate the hypothetical film properties. Lattice mismatch, magnetostriction coefficients, magnetization. damping and growth-induced and stress-induced anisotropies are calculated for any film composition from published data on standard compositions.

The magnetostriction coefficients (λ_{111} and λ_{100}), magnetization($4\pi M_s$) and the damping constant are calculated using the proportion of each of the rare earths and adjusting for the exchange (A) due to the tetrahedral-octahedral ion pairs. Each rare-earth has associated with it magnetization. damping and magnetostriction coefficients. so that the net value is the sum of the proportion of each constant. This net value is then decreased due to the exchange which is calculated from the iron dilution

The lattice mismatch is similarly calculated, however the dilution of the iron sites must be carefully considered. Typical iron substituents such as gallium and germanium have been installed in the program by using a quadratic equation describing the lattice reaction to the dilutant incorporation. The quadratic describes the probability of the ions residing at a tetrahedral site [a smaller site resulting in expansive stress] or an octahedral site [a larger site resulting in a compressive stress]. The equations are derived from fitting published data to a plot and digitizing the resulting curve.

The growth-induced anisotropy is calculated using the pair ordering model of large ion-small ion interaction. A constant K_{ij} is assigned to each pair of rare-earths so that the net growth-induced anisotropy is the sum of each K_{ij}-rare-earth product. (i.e, $K_G = K_{ij} X_Y X_{Lu}$ for Y-Lu pair). Anisotropy results from the pair ordering of Samarium and Europium with other rare-earths have correctly estimated published results. Using the lattice mismatch previously calculated, the stress-induced anisotropy is estimated and thus the total uniaxial anisotropy, K_u, is computed.

The inclusion of Bismuth in the films complicates the estimation of growth-induced anisotropy and the computer program produces mixed results. Bismuth appears not to behave as the pair-ordering model would suggest, but does have a large anisotropy. Bismuth incorporation into films is a sensitive function of growth temperature and additives to melt and thus a great variation of uniaxial anisotropy, more so than has been possible hitherto, is accomplished by just varying the growth parameters of the Bismuth melts

In order to use the program, the user is required to specify the desired bubble diameter and Q From these values, the values of A, K_u and $4\pi M_s$ can be determined from two standard bubble equations. First, the ratio of $K_u : 2 \cdot M_s^2$ is equal to Q

$$K_u \ 2\pi M_s^2 = Q$$

Secondly, the characteristic length is directly related to the bubble diameter, the exchange constant A, the anisotropy constant K_u and the magnetization, $4\pi M_s$

$$1 = \text{(bubble diameter)}/9 = 16 \, \pi \, (\, A \, K_u)^{1/2} \, / \, (4\pi M_s)^2.$$

Possible choice of constituents are picked, based on user's special needs (such as isotropic magnetostriction) and all compositions are scanned for possible useful compositions. Only those satisfying all requirements are retained and the ideal one is picked from this list.

The program is also capable of estimating physical properties of a particular film, given a film composition. This is especially useful in determining how the properties would change following melt alterations.

From the film composition, the melt composition is derived using the various segregation ratios that have been experimentally determined and reported in literature.

A typical output from using the computer program is shown in Table I and the best choice for an isotropic magnetostrictive film is shown by an asterik.

Section III LPE Film Growth Technique

All garnet growth is accomplished by the standard vertical dipping method. The growth takes place in a three zone vertical furnace with the crucible containing the melt in the center of the middle zone. With our new furnace, the three zones are controlled individually by different temperature controllers, so as to enable independent variation of temperature in the different zones. This results in better control of temperature and better temperature profiles. An insulating sliding door assembly on top of the furnace reflects the furnace heat at the top, for efficient heating.

Two types of melt-flux systems are used in our laboratory: $PbO\text{-}B_2O_3$ system and the new $PbO\text{-}Bi_2O_3$ system. The melt constituents are weighed, mixed and packed into a platinum crucible. For the Bismuth melts, platinum crucibles with twice the normal wall thickness had to be used to withstand the corrsion due to the melt. The melt is dissolved in the appropriate flux system and the solution is superheated to above saturation temperatures (T_{sat}) and allowed to homogenize for a minimum of 24 hours. It should be noted that in the Bismuth systems, Bi_2O_3 plays the dual role of flux and film constituent.

The films are grown by decreasing the temperature of the melt to below $T_{sat.}$ (typically around 870° C) and lowering a $Gd_3Ga_5O_{12}$ (GGG) substrate attached to a platinum substrate holder, rotating at 100 rpm, into the melt. The film will grow as long as the melt temperature is below $T_{sat.}$ and the mismatch between the film and the substrate is not too great; typically less than 0.03 A. The film is grown approximately 0.2 μm thicker than the bubble diameter, thus for a 1 μm diameter bubble film, the thickness would be around 1.2 μm. Typical growth rates (depending on the supercooling and melt additives) are 0.2 μm/min to 1.0 μm/min, so that the growth times vary from 30 seconds to about 5 minutes. Films with 0.5 μm bubble diameters. which are required to have a large Bismuth content are usually grown for short times. (around 30 seconds) After the film is grown, the substrate is raised above the melt surface and spun rapidly to get rid of excessive flux drops. Then the substrate holder is dismounted from the furnace and any remaining flux drops are dissolved.

A 40 % acetic acid, 10 % nitric acid and 50 % water solution proved effective for removing the PbO-B_2O_3 flux from the substrate and the substrate holder. This flux solution was found to be insufficient when removing the PbO-Bi_2O_3 flux used for growing the bismuth doped films. The flux removing solution was systematically altered to 40% acetic, 40% nitric and 20% water which proved to remove all of the remaining flux. During the flux removal procedure. the substrate, while mounted on the substrate holder, is alternately heated with a hot plate to 90° C and submerged in an ultrasonic bath.

Besides growing (111) films for device fabrication. several (100) films were also grown to measure their normal magnetostriction (λ_{100}) . The (100) films turned out to be relatively more difficult to grow due to greater adhesion of flux droplets to their surface

Section IV Film Characterization Technique

The films grown are characterized for possible melt alteration as well as to provide data for device work. Every film grown has its thickness measured. while most have the characteristic length and magnetization measured. Sample films are further characterized for lattice mismatch damping. gyromagnetic ratio. magnetostriction coefficients and H_k

The thickness measurements are made optically from a reflectance trace of the film. Using the

interference of the light reflected from the bottom surface and the top surface of the film, a reflectance trace of the film is made by varying the wavelength of the incident light. This trace is then used with a graph of the index of refraction of the film as a function of the wavelength of light, to determine the thickness. The wavelength dependence of the index of refraction in turn is determined by measuring the thickness of a representative sample of a lot accurately, using the Transmission Electron Microscopy technique. An alternate method was employed in verifying the film thickness measurements in case of thick films (thickness $> 5~\mu m$) and in deriving their index of refraction as a function of wavelength. A region of the film is etched part of the way (say, about 2 μm) and a surface profilometer is used to measure the difference in thicknesses between the etched and the unetched areas. This is compared to the corresponding value obtained using reflectometry trace in the etched and the unetched areas. Thus using reflectometry, thickness is measured in a fast, nondestructive manner. Typically, the thickness is measured at several points on the film surface to eliminate systematic errors and also to determine if there are surface imperfections such as mesas on the film.

Both the characteristic length, l and the magnetization $(4\pi M_s)$ are determined optically by domain observation under a polarizing microscope. Measurement of the domain stripe width. together with thickness can be used to determine l^5. Magnetization is determined by measuring the perpendicular field that causes the bubbles to collapse and using the ratio of stripe width to film thickness. Published tables relate the ratios of stripe width and film thickness to the ratio of collapse field and magnetization and to the ratio of l and film thickness[6].

Using Ferromagnetic Resonance. (FMR) we can calculate the gyromagnetic ratio. gilbert damping parameter, effective internal field (and thus the uniaxial anisotropy field) and the magnetostriction coefficients. The ferromagnetic resonance signals of the sample are found at various microwave frequencies and a graph of resonance frequency vs applied field is plotted. The slope of the curve for applied fields perpendicular to the sample, yields the gyromagnetic ratio. The intercept of the same curve, together with the value of magnetization, gives the uniaxial anisotropy field. The Gilbert damping parameter is related to the linewidth of the resonance signals. Furthermore, by applying a stress on the sample and thereby inducing a magnetostrictive energy, the FMR magnetic field is shifted to a different value. This shift is

related to the **magnetostriction** coefficients[7]. The resonance shift from the film on the back side of the substrate interferes with that of the epi-side and the backside of the film is therefore etched off prior to the measurement. Stress is applied on the sample mechanically by a vacuum applied on one side of the substrate. Under the present set-up, stress can only be applied normal to the sample and thus, (111) and (100) samples of the same composition are used to determine the respective λ constants. The magnetostriction coefficients are then used to evaluate the isotropicity of the samples.

The lattice mismatch is measured using a double crystal X-ray diffractometer. The X-rays penetrate approximately 4 μm into the garnet, thus going through the film to the substrate. Peaks are observed at the two angles corresponding to the substrate's lattice spacing and the film's lattice spacing. The difference of the angles is measured and used to determine the lattice mismatch. Thickness can also be approximated from the relative intensities of the peaks.

Section V Materials Development

In this section we review some of the materials developed in our magnetic bubbles facility. This section is intended to be a general overview and thus some materials are omitted from the discussion to keep it brief. Data from typical films discussed are shown in Table II.

Initially two submicron film compositions were developed. The first melt had the composition $Sm_{0.65}Gd_{0.28}Tm_{1.0}Y_{0.8}Lu_{0.27}Fe_{4.8}Ga_2$ with an l value of 0.056μm for a bubble diameter of 0.504 μm.

The second melt, producing films of $Sm_{1.2}Lu_{1.7}Tm_{0.1}(FeGa)_5O_{12}$ was also developed for submicron bubbles. This melt required significant alterations including an addition of gallium and iron to adjust the characteristic length, l, from 0.08μm to 0.06μm. The films were grown with a super cooling of 20 C and a T_{sat} of 880° C These films have been shown to successfully demonstrate propagation of 0.5μm bubbles in 2μm period contiguous disk devices

For useful contiguous disk devices the magnetostriction coefficients must be negative and as large as possible. Most rare-earth ions have λ_{111} less than λ_{100}, so that a balancing ion with λ_{111} greater than λ_{100} must be used. Two such ions that were investigated were dysprosium[8]

with $\lambda_{111} = - 5.90 \times 10^{-6}$ and $\lambda_{100} = - 12.60 \times 10^{-6}$ and bismuth with $\lambda_{111} - 15.50 \times 10^{-6}$ and $\lambda_{100} = + 8.20 \times 10^{-6}$. Thus dysprosium may be used without making the coefficients positive; however, dysprosium has a damping factor that is about forty times greater than the standard rare-earths. By using both dysprosium and bismuth together in a film, we are able to satisfy the isotropic magnetostriction requirements and have large negative magnetostriction coefficients and maintain a reasonable damping. Two sets of films were grown from two different flux based melts; the first melt was a dysprosium doped standard $PbO-B_2O_3$ flux melt and the second was a bismuth $PbO-Bi_2O_3$ flux melt.

The dysprosium film composition was $Sm_{0.3}Dy_{1.6}Gd_{0.4}Lu_{0.7}(FeGa)_5O_{12}$ which had magnetostriction coefficients of $- 2.8 \times 10^{-6}$ and a mismatch of less than 0.005 A. Films grown from this melt were however found not too well suited for device work.

The second isotropic melt was based on the bismuth system. The incorporation of bismuth into the film has several advantages including an increase of optical contrast due to an increase of the Faraday rotation[9], a secondary source of anisotropy and the correction of magnetostriction. Due to bismuth's positive magnetostriction coefficients, bismuth is used in small quantities as a correction to the magnetstriction. The greatest difficulty with using bismuth was that a new flux system must be developed employing $PbO-Bi_2O_3$ instead of $PbO-B_2O_3$. We have had little previous experience and no success with this system prior to this series of films.

We have grown films doped with bismuth of the general composition[10] $(\{Dy\ Sm\ Lu\ Y\ Bi\}_3\ FeGa_5\ O_{12})$ The magnetization of these films turned out to be larger than desired $(4\pi M_s = 1750$ G) and the bubble diameter at 0.35 μm. The magnetostriction coefficients were reasonably good with $\lambda_{100} = - 4.6 \times 10^{-6}$ and $\lambda_{111} = - 1.8 \times 10^{-6}$; the fact that λ_{100} is more negative than λ_{111} shows that the melt is overcompensated for isotropic magnetostriction.

The AK series melt is an improvement over this melt. Series of films with λ 's ranging all the way from undercompensated (λ_{111} more negative than λ_{100}) to isotropic composition were grown, with plans for overcompensated films in the future. These have good device properties. Devices made from the 0.5 μm films are discussed elsewhere in this report and the corresponding propagation margins and their temperature dependences etc. are also discussed therein.

AG and AH series melts were also bismuth melts for 1.0 μm films. These are essentially used for current access device fabrication, which is also discussed elsewhere in this report. These contain the same constituents as the 0.5 μm films but have different compositions. These too were designed to be isotropic and were found to be reasonably so.

A difficulty with bismuth films is the non-uniformity of the surface. This is due to the flux adhering to the film while being withdrawn from the melt letting the film continue to grow until the flux drops solidify. These flux drops result in a thicker film where the flux drops remain after withdrawl. Solving this problem was accomplished by adding Vanadium oxide to the melt so that the surface tension of the melt was increased while the melt viscosity was decreased[11]. Besides producing cleaner films, the addition of Vanadium also slowed the growth rates resulting in more uniform films. It has also been shown that addition of Vanadium increased the amount of bismuth incorporation into the films.

Films of the AF series are 1.0 μm non-bismuth type with composition $\{Tm\ Sm\ Lu\}_3[FeGa]_5(O)_{12}$ and are used for fabricating devices using silicon on garnet technology, which too is described elsewhere in this report.

Section VI Temperature Studies

In order to be useful in practical applications, these isotropic IICD devices must be able to perform in a wide range of ambient temperature. Bubble devices are designed to operate in the extended temperature range of -50° C to + 150° C. The temperature dependence of the properties of the isotropic bubbles that are grown here are being studied currently and preliminary results are reported here.

The important bubble device parameters whose temperature dependences need to be studied are (1) Bubble collapse field, H_c (2) Bubble diameter and (3) isotropy, λ_{111} - λ_{100} to ensure isotropic propagation at all temperatures of operation. The bubble collapse and bubble diameter are measured by direct observation under a microscope, as mentioned earlier. To study the temperature effects, an experimental set-up as shown in Fig. 1 is used. The magnetic bias field is provided by a set of flat 'pancake' coils on which a thermoelectric heater is mounted. Thus the heating is localized at the sample with no associated problems of the magnet heating up The

thermoelectric heater covered a reasonably wide range of temperature ($\sim$ -20 ° C to -120 ° C) For greater range of temperature, we plan to use an insulating chamber on top of the bias field assembly, enclosing the heater and to circulate temperature-controlled nitrogen gas (from evaporating liquid nitrogen). The decrease in the bubble collapse field with temperature in typical bubble films is designed to match the rate of decrease in the rate of decrease in the field values of most commercially available Barium ferrite permanent magnets, which is the source of the bias field. This is about 0.2 % per degree C, in the 20 - 60 ° C range. Preliminary data taken on a 1.0 μm bubble film for H_c is shown in Fig. 2 and it is seen that H_c decreases at an almost similar rate. Such temperature studies are being currently carried out on 0.5μm samples and the data is not complete at present.

Section VII Current and Future work

Currently, work is being done in several areas. On the film growth front, overcompensated films are being grown and devices grown on these films will be evaluated for their performance at room temperature and over a temperature range. Studies are also being carried out to see how the film properties, especially the magnetostriction coefficients, depend on the growth temperature.

Evaluating better temperature dependences is going to be taken up next. Instrumentation for measurement over a large temperature range is being planned. Plans are also being made to adapt the FMR set-up for temperature measurements so the magnetostriction coefficients can be evaluated as a function of temperature. The study of propagation margins as a function of frequency of the isotropic films will be taken up. Materials aspects of such parameters as gilbert damping parameter etc. will also be studied. Controlling and optimizing the various film growth parameters to yield the highest quality films will always be a part of any of our future endeavor

References

[1] Y.S. Lin, G.S. Almasi, D.B. Dove, G.E. Keefe, and C.C. Shir, "Orientation dependence of propagation margin of 1-μm bubble contiguous-disk devices -- Clues and Cures", *J. of Appl. Phys.*, 50, 2258, (1979).

[2] R. Wolfe, T.J. Nelson, "Crystal Symmetry Effects in Ion-Implanted Propagation Patterns for Magnetic bubbles: 'Roof-Top' Designs", *I.E.E.E. Trans. Magnet.*, MAG-15, 1323, (1979).

[3] A. Hubert, "Domain Wall Phenomenon in Bubble Propagation Layers", *J. of Magnetism and Magnetic Materials*, 35, 249, (1983).

[4] M.H. Kryder, D.A. Saunders, "The Effects of Stress Relaxation and Anisotropic Magnetostriction On Charged Walls in Ion-Implanted Garnets", *I.E.E.E. Trans. Magnet.*, MAG-19, 1817, (1983).

[5] A. H. Eschenfelder, *Magnetic Bubble Technology*, Springer-Verlag, New York, (1980).

[6] D. C. Fowlis and J. A. Copeland. AIP Conf. Proc. 5, 240, (1972).

[7] X. Wang, C.S. Krafft. M.H. Kryder. "Measurement of Magnetocrystalline Anisotropy Field and Magnetostriction Coefficient in Garnet Films", *I.E.E.E. Trans. Magnet.*, MAG-18, 1295, (1982).

[8] H. Makino, O. Okada, and Y. Hidaka. "Dysprosium Containing Bubble Garnet Composition for Ion-Implanted Contiguous Disk Devices", *J. Appl. Phys.*, 55, 2551, (1984).

[9] P. Hansen, K. Witter, and W. Tolksdorf. "Magnetic and Magneto-optic Properties of Lead- and Bismuth-Substituted Yttrium Iron Garnet", *Phys. Rev.*, B27, 6608, (1983).

[10] R. O. Campbell, Masters Thesis, Carnegie Mellon University, 1985.

[11] Y. Hosoe, K. Andoh, T. Ikeda and R. Suzuki, "Reduction of Growth Rate in Bi-substituted Bubble Garnets Using MoO_3 and V_2O_5 Added Flux", *I.E.E.E. Trans. Magnet.*, MAG-22, 1200. (1986).

List of Tables

Composition

	$4\pi M_s$ [G]	Δa_o [A]	λ_{111} $[10^{-6}]$	λ_{100} $[10^{-6}]$	$\lambda_{111}\text{-}\lambda_{100}$ $[10^{-6}]$	K_g	K_s $[10^4\,erg/cm^3]$	K_u
$Bi_{0.20}Dy_{1.00}Sm_{0.20}Lu_{0.90}Y_{0.70}Fe_{5.00}Ga_{0.00}O_{12}$								
	1340	0.001	-2.78	-3.00	0.22	6.4	0.14	6.5
$Bi_{0.30}Dy_{0.80}Sm_{0.20}Lu_{1.10}Y_{0.60}Fe_{4.90}Ga_{0.10}O_{12}$								
	1300	0.000	-1.85	-1.83	-0.02	8.4	0.01	8.4
$Bi_{0.40}Dy_{0.60}Sm_{0.20}Lu_{1.20}Y_{0.60}Fe_{4.80}Ga_{0.20}O_{12}$								
	1270	0.002	-1.00	-0.78	-0.23	10.2	0.06	10.2
$Bi_{0.40}Dy_{0.70}Sm_{0.20}Lu_{1.30}Y_{0.40}Fe_{4.84}Ga_{0.16}O_{12}$ *								
	1280	0.000	-1.13	-1.14	0.00	10.3	0.01	10.4
$Bi_{0.50}Dy_{0.60}Sm_{0.20}Lu_{1.50}Y_{0.20}Fe_{4.78}Ga_{0.22}O_{12}$								
	1260	0.001	-0.46	-0.48	0.02	12.3	0.01	12.3

Table 1: Calculated Properties of $\{DySmLuYBi\}_3 FeGa_5(O)_{12}$ films with isotropic magnetostriction, bubble diameter. 0.5 μm.

film number	h (μm)	l (μm)	$4\pi M_s$ (G)	Rate (μm/min.)	Temp. ($^\circ$C)
$Sm_{0.3}Gd_{0.4}Tm_{0.73}Y_{1.57}Fe_{4.4}Ga_{0.6}O_{12}$					
207	1.98	0.159	586	0.33	854
208	1.64	0.146	593	0.33	838
$Sm_{1.2}Lu_{1.7}Tm_{0.1}(FeGa)_{5.0}O_{12}$					
AC21	1.21	0.001	1230	0.24	860
AC22	1.29	0.059	1134	0.26	868
$Y_{2.8}La_{0.2}Fe_{3.7}Ga_{1.3}O_{12}$					
AD03	1.20	---	---	0.20	860
AD41	3.20	0.144	220	0.32	880
$\{Dy\ Sm\ Lu\ Y\}_3Fe_5O_{12}$					
BA01	1.25	0.044	1765	0.25	885
BA03	1.40	0.0395	1730	0.47	863
$\{Tm\ Sm\ Lu\}_3[FeGa]_5O_{12}$					
AF23	1.096	0.138	668	0.254	833
AF26	1.50	0.1308	667	0.25	834
$\{Sm\ Lu\ Bi\ Y\ Dy\}_3[FeGa]_5O_{12}$ 1.0 μm.					
AG42	0.839	0.228	353	0.606	903
AG43	1.349	0.144	438	1.614	875
$\{Sm\ Lu\ Bi\ Y\ Dy\}_3[FeGa]_5O_{12}$ 1.0 μm.					
AH47	1.19	0.119	576	---	945
AH48	1.15	0.112	555	---	945
$\{Sm\ Lu\ Bi\ Y\ Dy\}_3[FeGa]_5O_{12}$ 0.5 μm)					
AK51	0.82	0.0526	1077	1.89	871
AK53	0.77	0.0549	1125	2.01	868

Table 2: Typical film properties

List of Figures

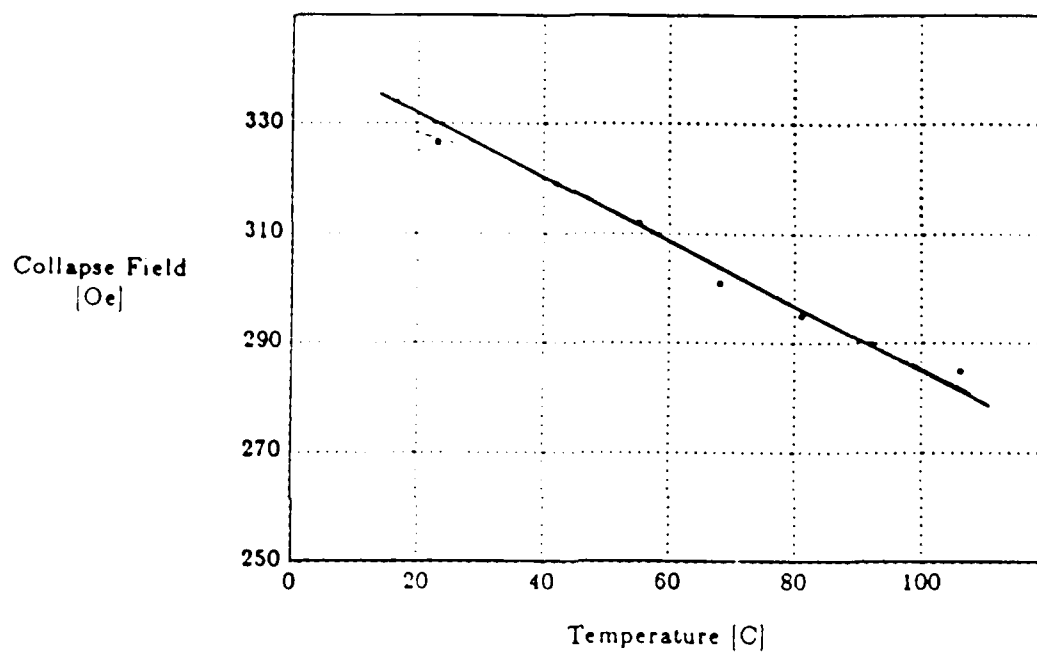**Figure 1:** Experimental set-up for temperature studies of H_c

Figure 2: H vs Temperature for sample AH 39

Current-Access Ion-Implanted Magnetic Bubble Devices

Michael Alex and Mark H. Kryder
Department of Electrical and Computer Engineering

Abstract

A bubble propagation device based on the combination of ion-implanted devices and current-access devices is presented. Experimental results show that the potential well experienced by a bubble in these hybrid devices is greater than in either device alone. In addition, by utilizing the charged wall of the implanted structure the minimum drive current of the hybrid device is reduced by a factor of two when compared with the current-access device. A computer model used to calculate the enhanced well depth of the hybrid device accurately predicts the experimental results.

Introduction

The current-access ion-implanted bubble device is a hybrid of two very different magnetic bubble propagation structures: the ion-implanted or contiguous disc device and the current-access or perforated sheet device. In this report the device is introduced and its method of operation is described. Computer simulations are performed comparing actual hybrid device data with that expected from the theory. There is excellent agreement between the experimental and computed results.

The Device Structure

The current-accessed ion-implanted device structure is depicted in Fig. 1. It consists of a planar current sheet with a circular aperture; the area under the sheet is ion-implanted while in the aperture the magnetization remains normal to the film plane. Thus, except for the current sheet the device looks just like a basic contiguous disc propagation structure.

Current flow through the sheet has two effects. First, the in-plane magnetic field component produces charged walls at the positions shown in the figure. At these same positions potential wells due to the normal magnetic field component are created. Note
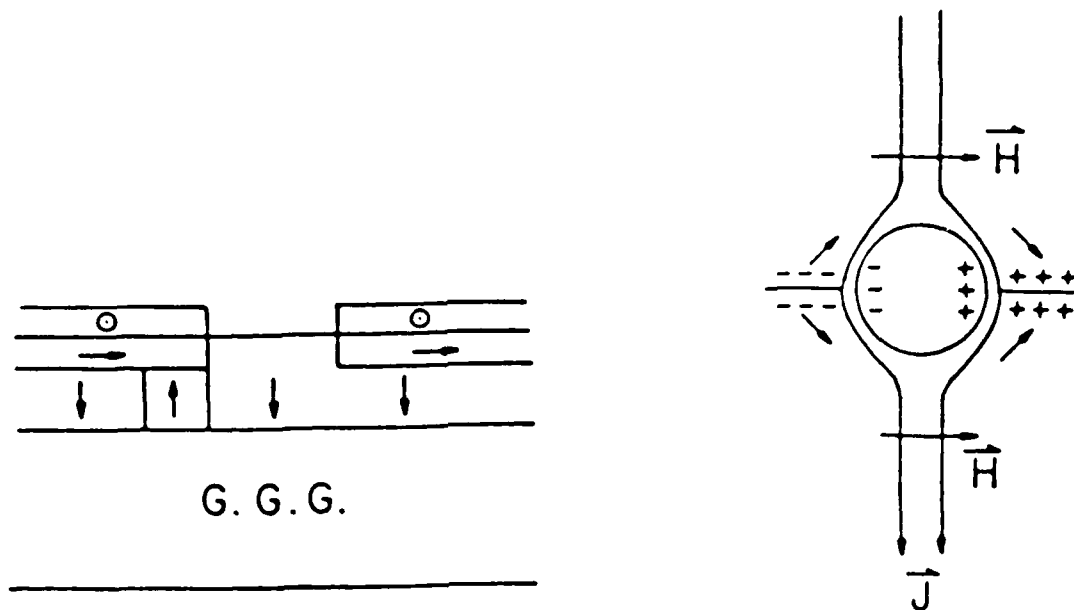
Figure 1: Cross-section and Top View of the Current-Access Ion-Implanted
Bubble Device

that rotating the current will rotate the charged walls and the potential wells in phase
with each other. In the figure a bubble is coupled to an attractive charged wall; this is
also the location where the bias field is minimized, further enhancing bubble stability.
Rotating the current in the film plane will result in the rotation of the bubble due to
charged wall rotation as well as the bias field gradient in the same direction. The
bubble, in essence, is driven independently by the two different mechanisms mentioned
above.

One may measure the merits of each of these driving forces (the bias field gradient
and the charged wall) by measuring the collapse field of a bubble as it is under the
influence of each of these mechanisms. This measurement yields the "potential well"
that the bubble experiences; the deeper the well the higher the collapse field and the
more stable the bubble is. These measurements, as well as others, are presented in the
next section.

Experimental Results

In the work of Ohta and Kryder[1], a 1μm bubble was placed in the vicinity of an aperture with a radius of 4μm. With a current density J mA/μm flowing through the conductor, the bubble was attracted to the potential well as described above. The depth of the well was measured as a function of J by measuring the collapse field of the bubble at this location. The results are presented in Fig. 2. The collapse field increases linearly with increasing current density. At J $= 0$, the collapse field is 346 Oe. At a current density of 2mA/μm, the collapse field increases to 356 Oe.
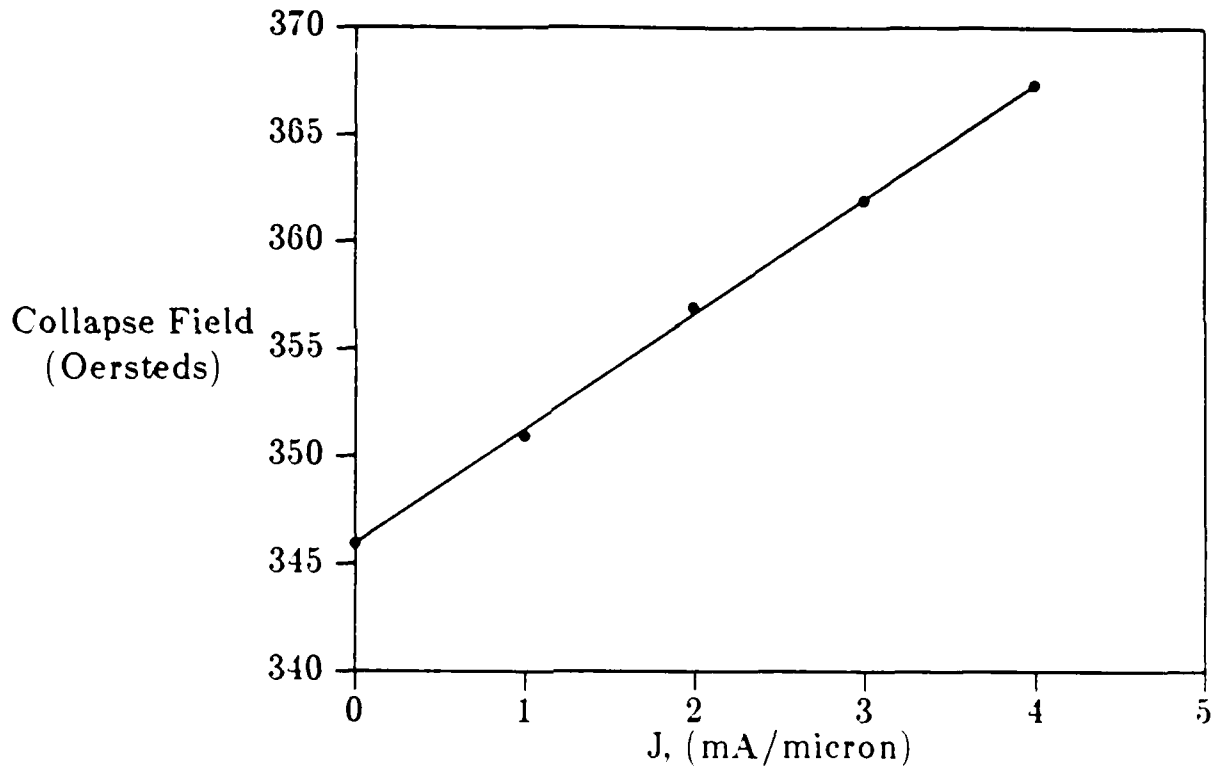
Figure 2: Bubble Collapse Field of Current Access Structure

For the ion-implanted structure, the bubble collapse field may be measured as a function of an applied in-plane field in order to obtain an estimate of the potential well

depth. For a bubble coupled to an unimplanted disc, there are "stable" and "unstable" bubble positions. Bubbles will reside at stable positions with no applied field; under the influence of an in-plane field however, the charged wall will stabilize a bubble at any position on the disc, even a previously unstable one. As seen in Fig. 3, the potential well characteristics of stable and unstable positions are different. For a bubble attached to the stable position, the collapse field decreases monotonically as the in-plane field increases. At the unstable position, the collapse field of the bubble increases, reaches a maximum and then decreases.
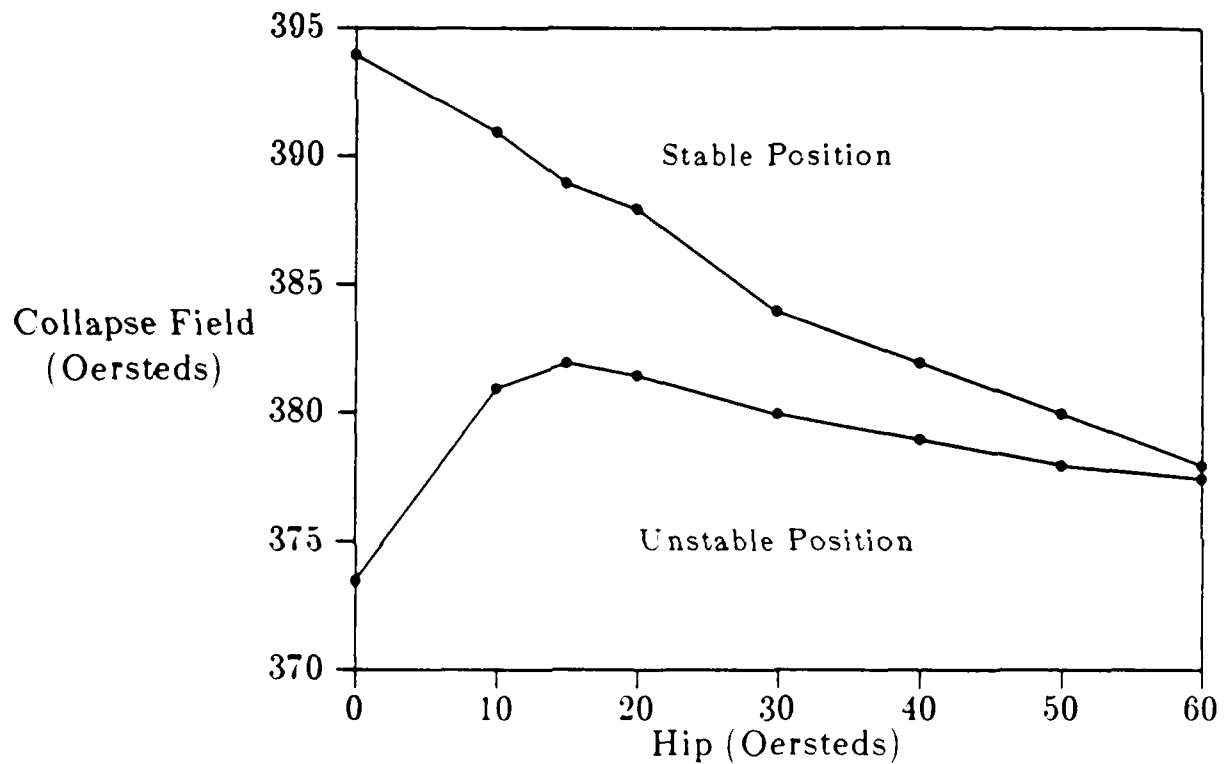
Figure 3: Bubble Collapse Field of Contiguous Disc Device Structure

Static characteristics of the ion-implanted current-accessed device are shown in Fig. 4. Recall that this device consists of an unimplanted disc underneath a current sheet

aperture of equal radius. As in the current-accessed device above, the collapse field of the bubble at a stable position was measured as a function of J, the current density through the sheet in mA/μm. As seen in the figure the collapse field at first increases linearly as in the current access device, and for current densities above 2.5mA/μm decreases hysteretically.
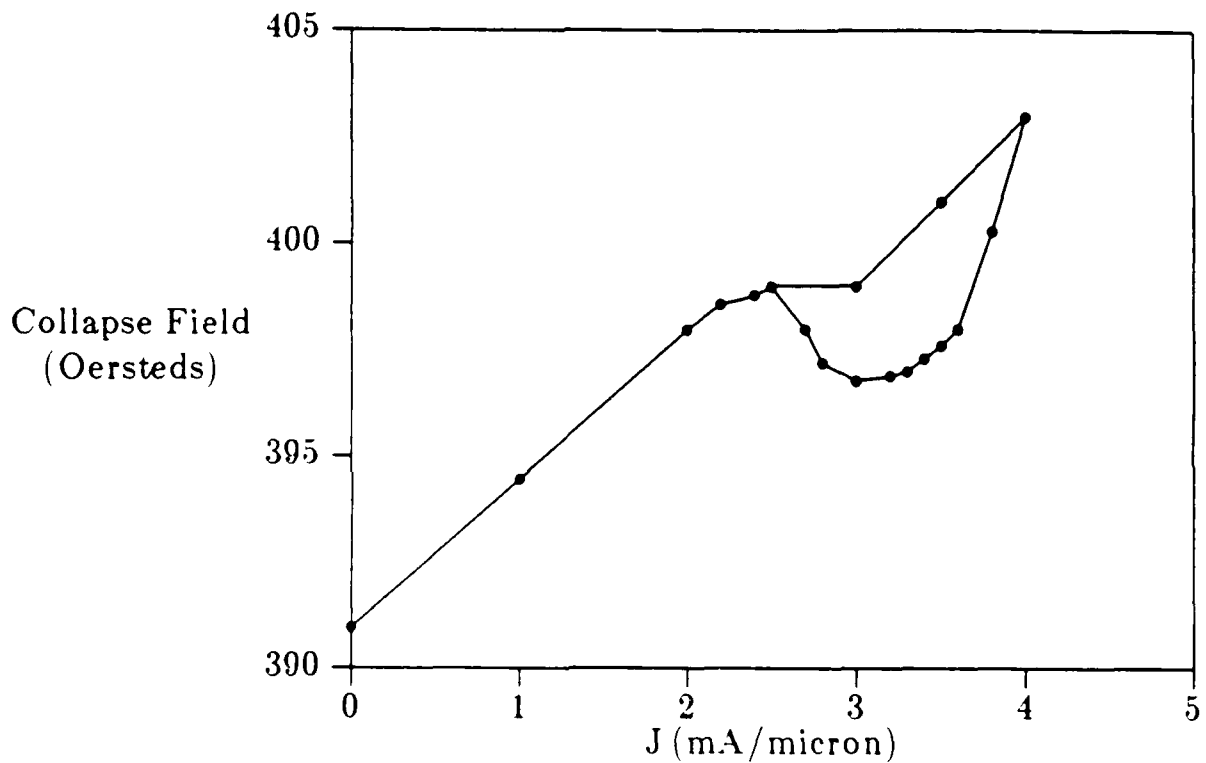

Figure 4: Bubble Collapse Field of Hybrid Device Structure

Another bubble device figure-of-merit and one that is pertinent for propagation structures is the bias field of circulation. In this experiment the bubble is circulated around an aperture at constant drive current and the bias fields at which the bubble strips out and collapses are measured. The better the device, the larger the range of bias fields expected. One would also like to minimize the drive current for circulation

at the same time. The bias field margins for circulation of a bubble around a 6μm current-access aperture and a 6μm hybrid device are seen in Fig. 5. Note that the hybrid structure has significantly better margins, and in particular, that the minimum drive current of the hybrid device is roughly one half that of the conventional current-access device. Since the power dissipation per unit device area is proportional to the square of the drive current, the hybrid device requires one quarter the power of the conventional structure.
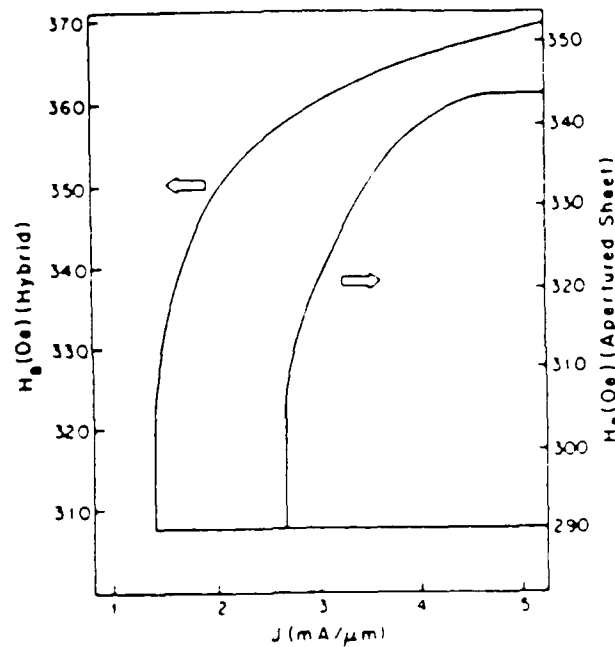
Figure 5: Current Access and Hybrid Device Circulation Margins

Finally, it should be noted that in the hybrid device, the drive field coils of conventional field-access devices have been eliminated. These coils are highly inductive and dissipate much power, especially at high frequencies. Through their elimination, these novel bubble devices will be capable of propagating bubbles at very high frequencies at low power consumption levels.

Discussion

In this section computed fields and bubble behavior expected from these fields are presented and compared to the experimental results.

The simple current-accessed device will be discussed first. In the data of Fig. 2, it is seen that the bubble collapse field increases linearly with current density, as is to be expected. Using the geometry of the experimental device, magnetic fields were calculated and the perpendicular field component (which is responsible for the increase in bubble stability) was added to the bubble collapse field at $J = 0$. In other words the collapse field of the bubble in the current-access device, $B_{c, cad}$ should be equal to the free bubble collapse field B_o (a constant) plus the perpendicular field from the current sheet aperture, B_p. The experimental and calculated results are shown in Fig. 6. Actually, in Fig. 6, the constant free bubble collapse field has been subtracted from the measured collapse field values of the current-access device; that is, del $B_o = B_{c, cad} - B_o$.

In the hybrid ion-implanted current-accessed device the situation is more complex. First, as has been demonstrated, is the fact that the perpendicular field increases the collapse field of a bubble as a linear function of current density. In the Experimental section, it was seen that for a bubble coupled to a charged wall in a stable position around an unimplanted disc the collapse field *decreases* as the in-plane field is increased. Thus, for the static case of a bubble in the stable position of the hybrid device, two competing effects are occuring as J is increased: 1) the perpendicular field component is increasing the potential well, and 2) the in-plane field component is decreasing the potential well. The net result is seen in Fig. 4.

One may calculate the expected potential well depth of the hybrid device (as a function of J) by adding to the decreasing well depth of the ion-implanted structure the increasing well depth due to the perpendicular field component. In Fig. 7 is the net collapse field that results along with the previous experimental results. The computed result is actually the experimental bubble collapse field of the ion-implanted device that has been augmented by the perpendicular field component from the current sheet.
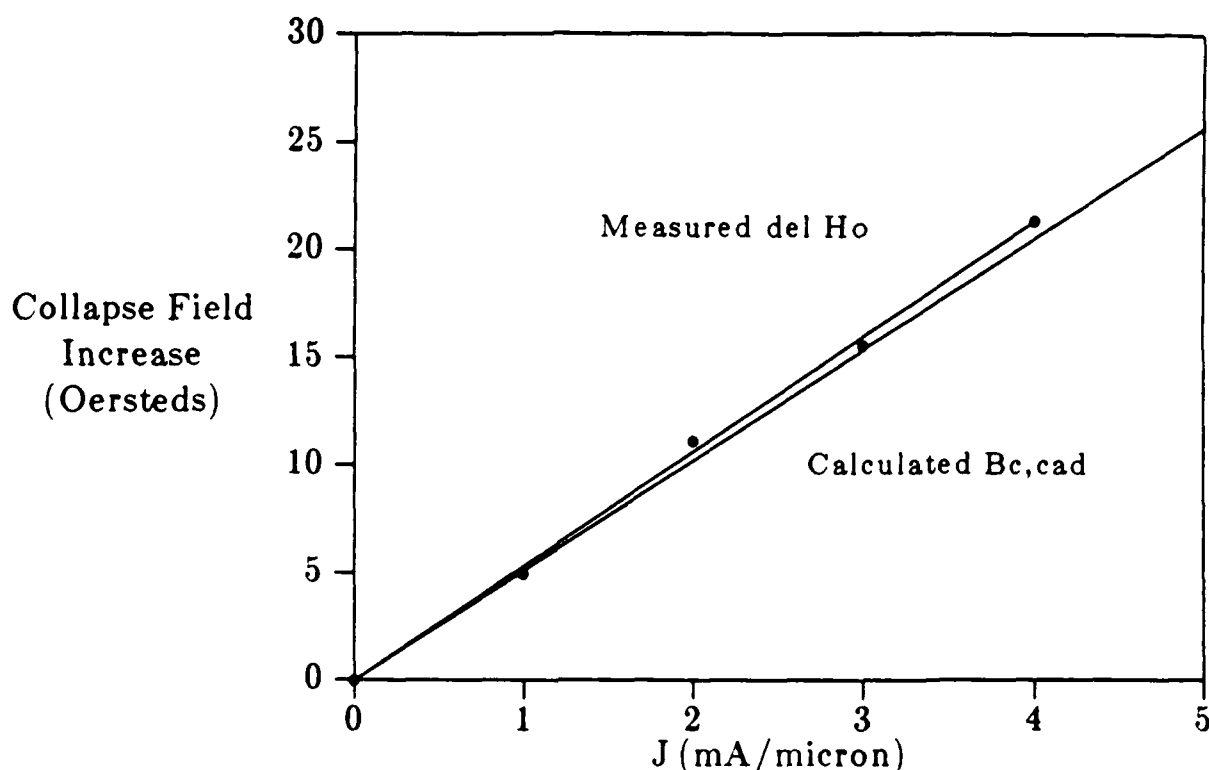
Figure 6: Calculated Perpendicular Field, B_z, and increase in
bubble collapse field of the Current Access Device

Present And Future Work

Although bubble circulation experiments indicate improved performance of the hybrid device over normal current-access devices, bubble propagation is required for practical memories. Thus, the concept of the hybrid aperture has been extended to the design of bubble propagators that behave much like contiguous disc devices but are driven by perforated current sheets. A typical design is seen in Fig. 8. Mask sets have been designed and written in order to fabricate these devices; device processing has been completed and at the time of this writing propagation structures are in the preliminary stages of testing. A mask set includes the ion-implanted level, perforated conductor levels as well as a bubble nucleator level. In addition, ion-implantation conditions have been established by measuring propagation margins of contiguous disc device structures.
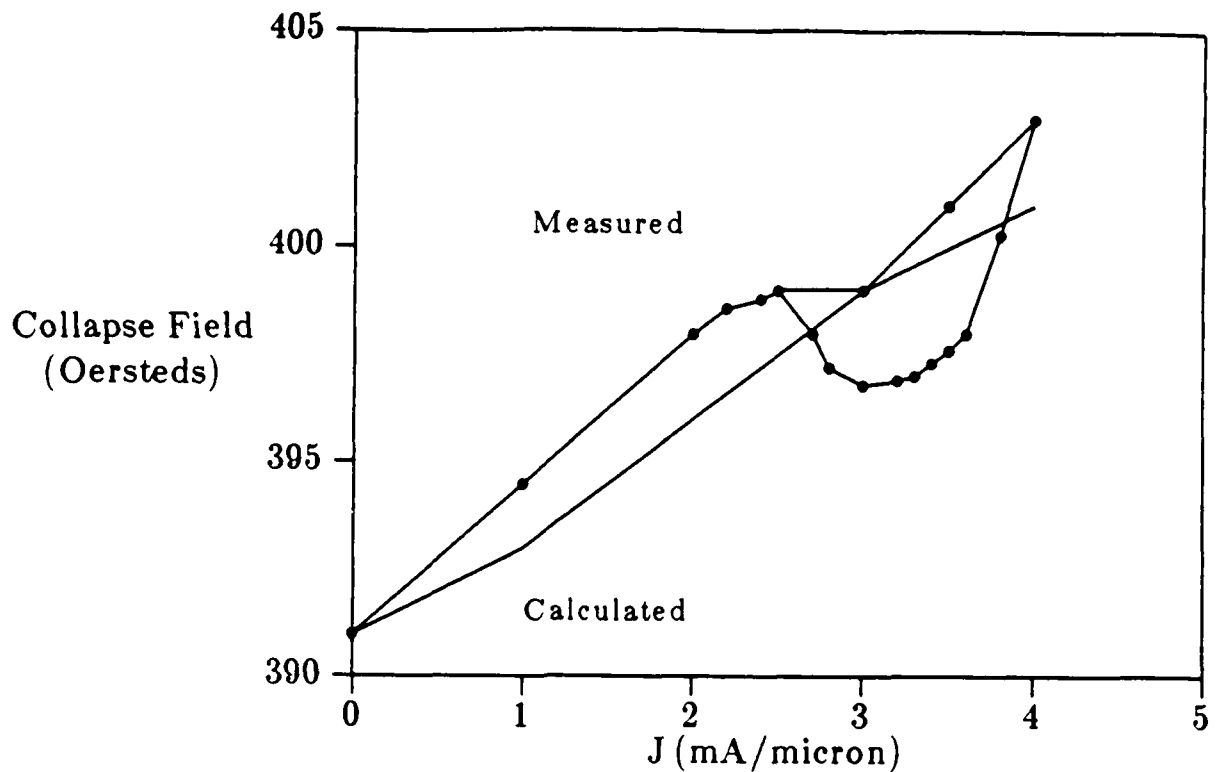
Figure 7: Calculated and Experimental Bubble Collapse Fields of the Hybrid Device.

The field calculations have been modified to include the influence of adjacent apertures, an important effect when the apertures get close, as in small bubble or high density configurations. For example, in Fig. 9 is seen the perpendicular magnetic field at the edge of an aperture of radius r as a function of angular position, phi (in radians), around the aperture with center-to-center spacing of an approaching aperture, r_{ij} as a parameter. In this figure, the values of r_{ij} are 2.5r, 3.0r, 4.0r, 10.0r and 50.0r. The magnetic field has been normaliz d to 2π. One can see that at $r_{ij} = 2.5r$ the sign of the potential well changes polarity and that two "satellite" wells are formed. The implications of this effect as well as other aspects of the device and its structure are presently being studied.
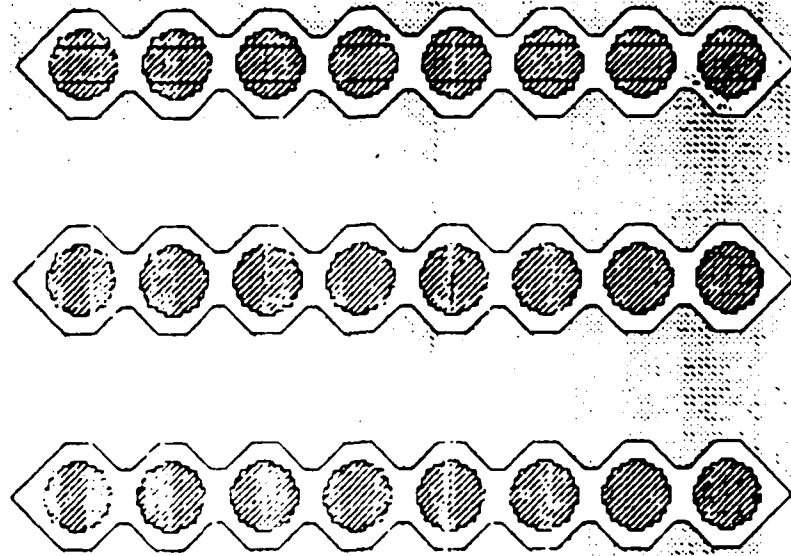
Figure 8: A Hybrid Device Propagation Structure

Device Simulation

In order to build a foundation for modelling and simulation of bubble motion in propagation structures, the model of Calhoun was utilized as a starting point.[7] In his work, Calhoun simulated the motion of a bubble driven by a charged wall circulating about an unimplanted disc. A schematic of the situation is depicted in Fig. 10. Several assumptions are used to simplify the analysis. It is assumed that the bubble and charged wall are rigidly coupled and that all the damping of the moving charged wall/bubble system is due to the bubble. Experiments have borne out the latter assumption to be correct.[9] The damping force of the bubble may be approximated as

$$F_d = \pi d M_s t_s (R/\mu_w) d\theta/dt, \qquad\qquad 1$$

where μ_w is the wall mobility of the storage layer, t_s is the storage layer thickness, M_s

Bz/2pi (Oe)
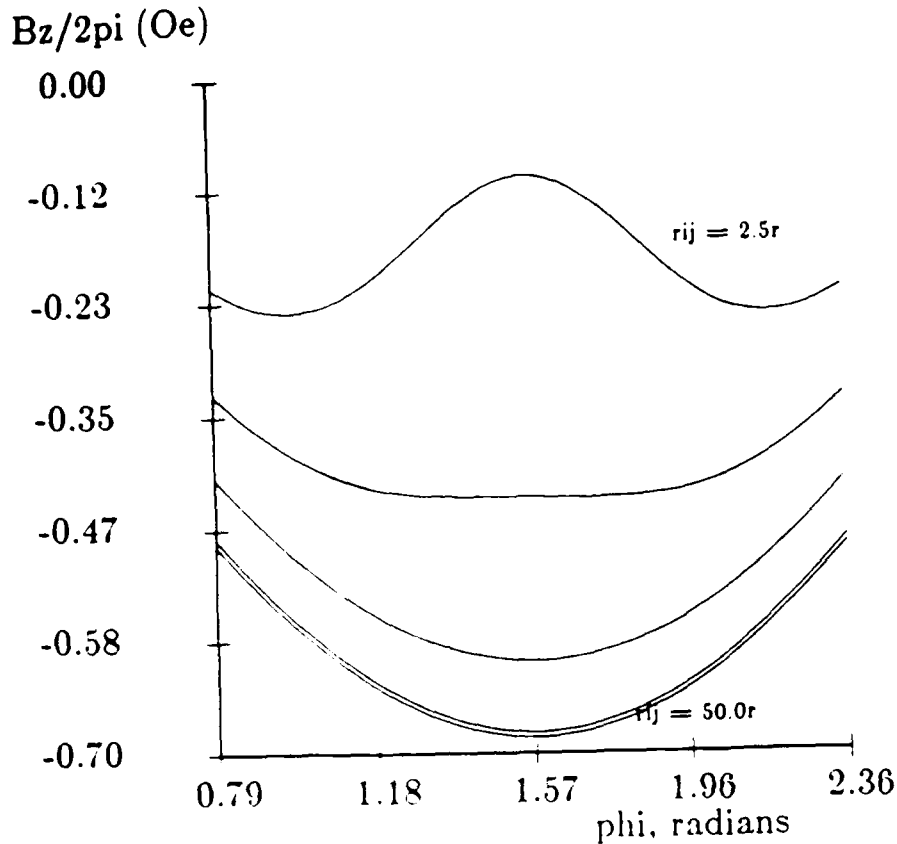
Figure 9: The effects of aperture separation on the perpendicular magnetic
field of an aperture of radius r. The values of r_{ij} shown are 2.5r.
3.0r, 4.0r, 4.0r, 10.0r and 50.0r. Phi is the angular position around the
aperture in radians. The current is incident at phi = 0.

is the magnetization of the storage layer, R is the radius of the bubble trajectory and i
is the bubble diameter.

The bubble/charged wall is driven around the disc by the applied field, H_{xy}. To first
order, we may approximate the charged wall as a sheet of length L, height t_d, the
thickness of the ion-implanted drive layer, having a uniform charge density $\rho =$
$2M_d \cos\alpha$, where α is the angle between the wall normal and M_d, the drive layer
magnetization. Then, the force due to H_{xy} driving the wall F_H may be given by:
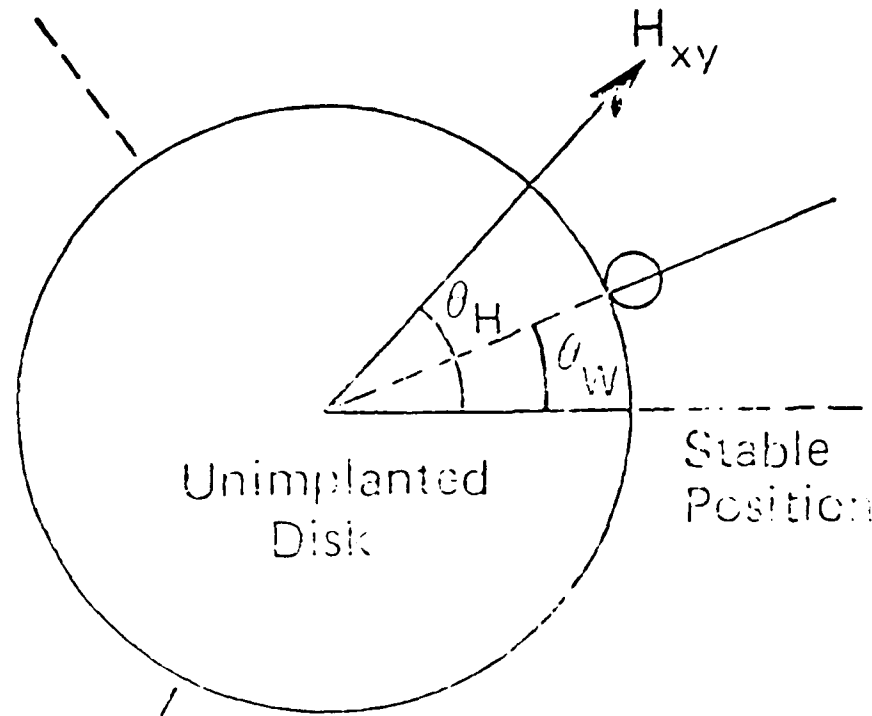
Figure 10: Charged wall/bubble circulating about an unimplanted disc.

$$F_H = (2M_d t_d L \cos\alpha)H_{xy}\sin(\theta_H - \theta_w) \qquad\qquad 2$$

where θ_H is the angle of the applied field and θ_w is the angular position of the wall and bubble.

In ion-implanted devices of the type described here, crystalline and stress- induced anisotropies play major roles in affecting charged wall behavior. The major component, the stress-induced anisotropy, has the same angular dependence as the crystalline anisotropy and is proportional to $\sin3\theta_w$. The form of these anisotropies gives rise to the three "easy" and "hard" directions of these devices; the charged wall will prefer to reside at $\theta = 0°$, $120°$ or $240°$. The restoring force is then given as:

$$F_r = (2M_d t_d L \cos\alpha)(H_{eff}/3)\sin3\theta_w. \qquad\qquad 3$$

where H_{eff}, the effective anisotropy field due to crystal symmetry and stress relaxation is:

$$H_{eff} = 9\sqrt{2}[(1/3)K_1 + (\lambda_{111} - \lambda_{100})(\sigma_n - \sigma_p)]H_B/[(Q_d - 1)4\pi M^2], \qquad\qquad 4$$

where Q_d is the quality factor of the implanted layer, H_B is the applied bias field, the λ's are the appropriate magnetostriction constants and σ_n and σ_p are the stress components normal and parallel to the implanted edge respectively. Note that for equal magnetostriction constants there is no contribution to the anisotropy field due to magnetostriction.

By equating the driving force with the restoring and damping force, $F_d + F_r = F_H$, we get the following first order non-linear differential equation:

$$v\, d\theta/d\omega t + 1/3\, \sin 3\theta = h\, \sin(\omega t - \theta), \qquad\qquad 5$$

where $h = H_{xy}/H_{eff}$, $v = R\omega/\mu_e$, $\theta_H = \omega t$ and $\mu_e = \mu(2M_d t_d L\cos\alpha)/\pi dM_s t_s$.

A computer program was written to solve the equation of motion by the Runge-Kutta method.[10] Two useful results obtained are 1), the position of the charged wall/bubble as a function of the in-plane field position, and 2), the phase lag between the drive field and the charged wall/bubble. In addition, the effects of drive field magnitude, stress and magnetostriction constants, operating frequency and dynamic bubble parameters on bubble circulation may be modelled.

In Fig. 11 is seen the bubble position around an unimplanted disc for two different values of the normalized in-plane field. Note that as the in-plane field is increased, the bubble follows the field more closely. This is seen more graphically in Fig. 12, which depicts the phase lag between the circulating bubble and the rotating in-plane field. For very high drive field values, the phase lag is virtually eliminated, as is seen in the laboratory.

It is interesting to see the effects on bubble motion due to having a material which is isotropic, that is the effects of the crystalline anisotropy and anisotropic magnetostrictive effect essentially neutralize each other. Referring back to equation 4
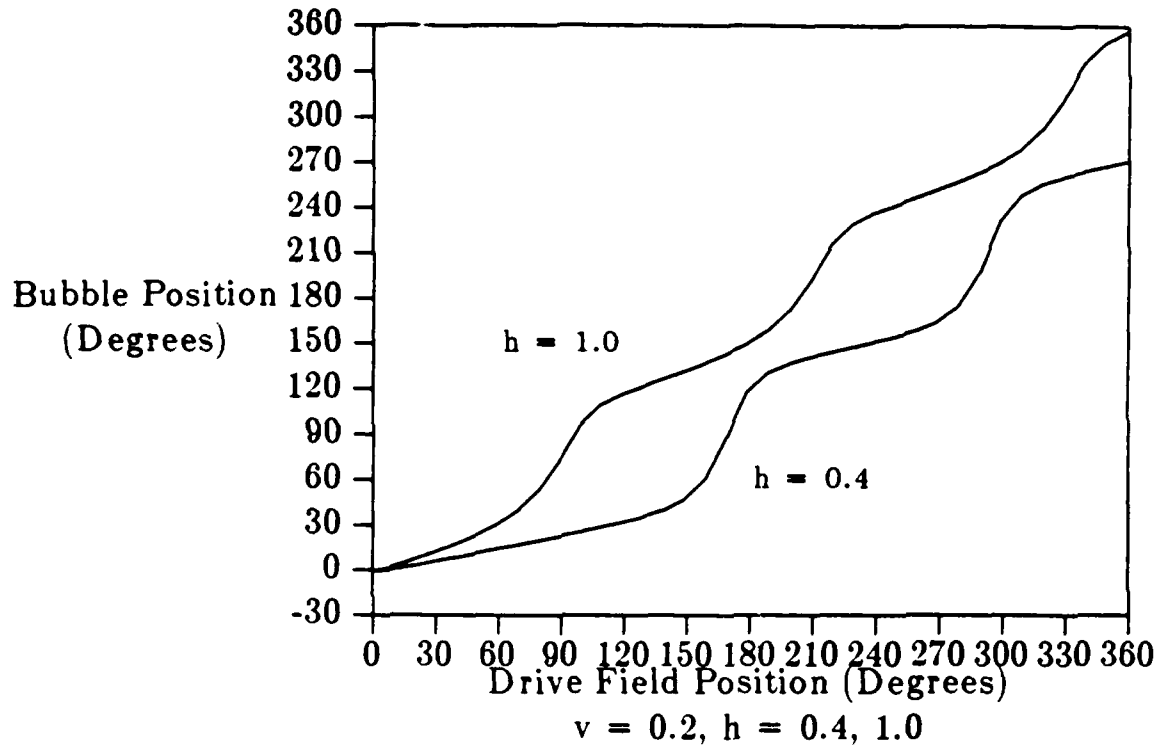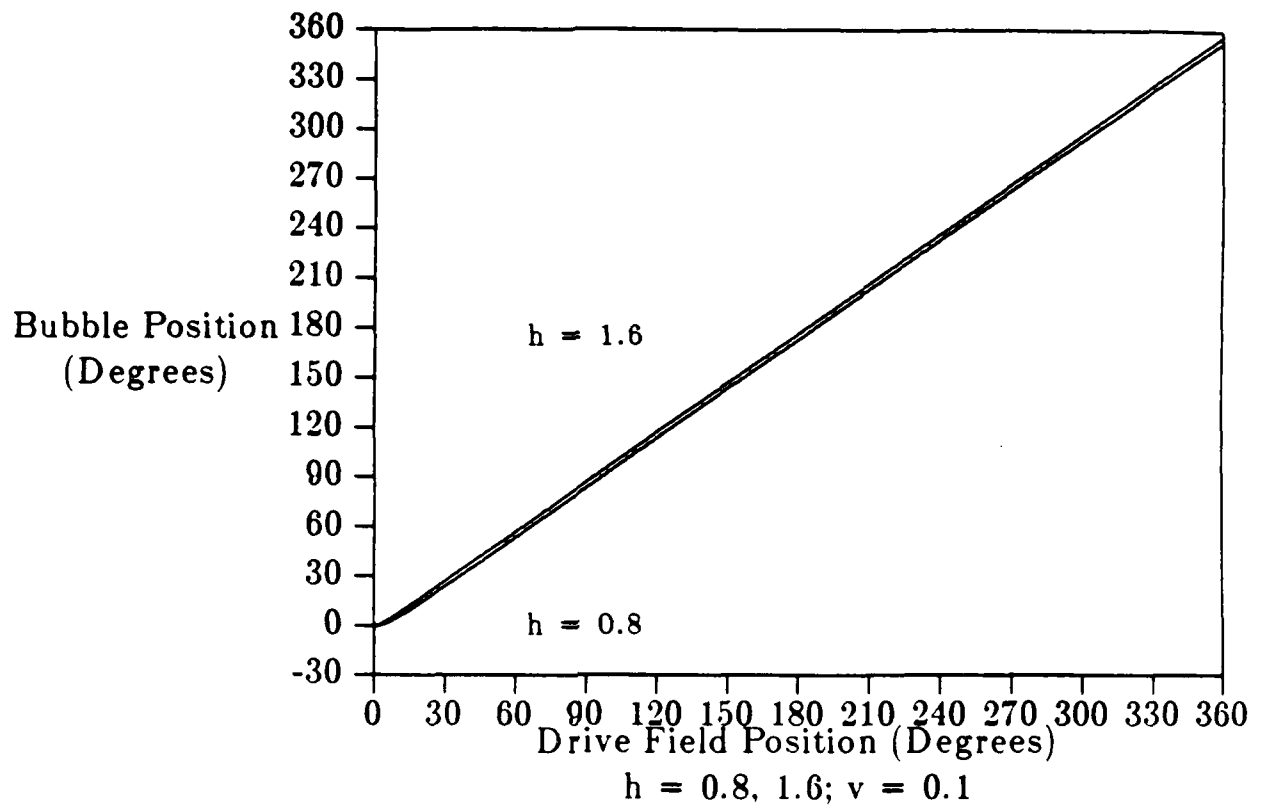
Figure 11: Bubble position as a function of drive field position around an unimplanted disc for two different values of the normalized drive field, h.

above, it is seen that a judicious selection of the magnetostriction coefficients, λ_{111} and λ_{100}, as well as knowledge of the stress distribution around the unimplanted disc can yield $H_{eff} = 0$. The simulated motion of a bubble in this case is depicted in Fig. 13 for two values of the normalized drive field, h. There is still a slight phase lag but it is constant, and the bubble's angular velocity, the derivative of the bubble position with respect to time, is also constant. This is certainly required for improved device operation and gives greater flexibility to the device designer who will not be restricted to limited propagation track geometries and orientations because of anisotropic bubble behavior.
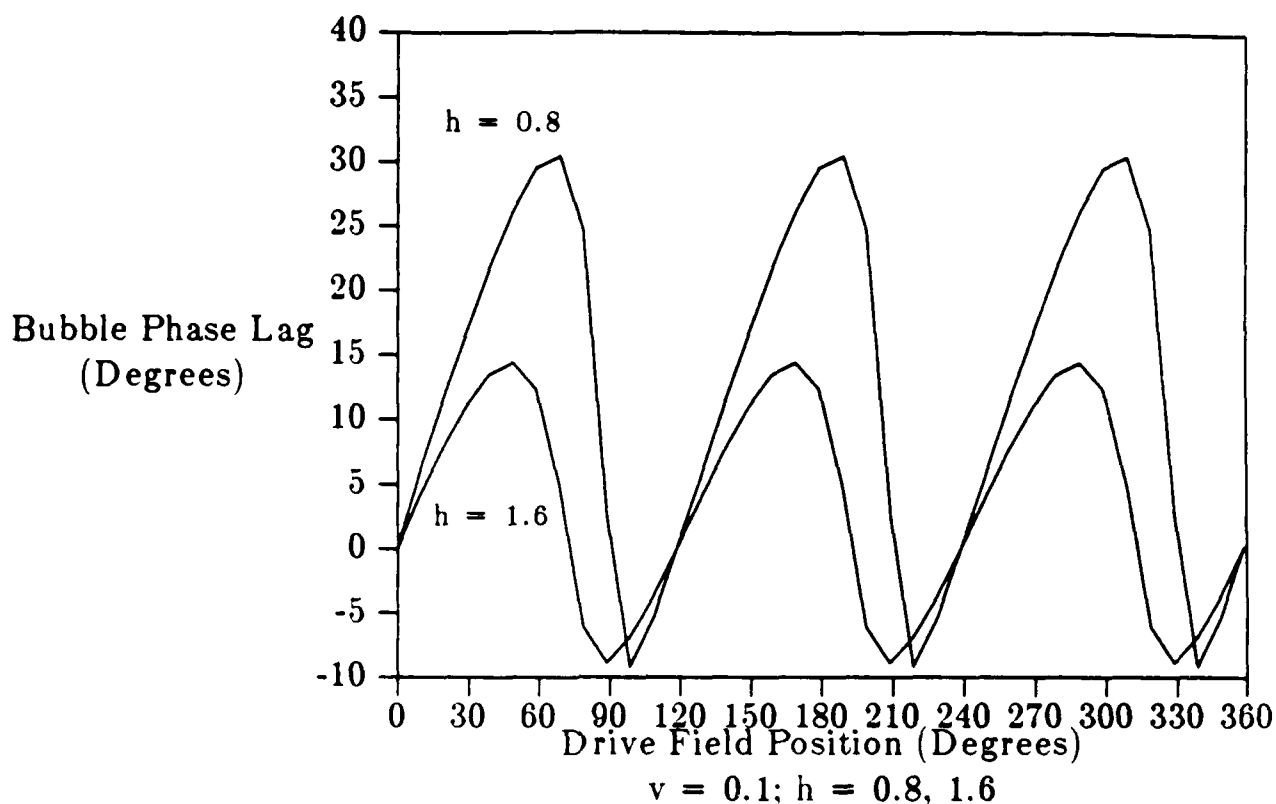
Figure 12: The phase lag between the drive field and circulating bubble for two different values of the normalized drive field, h.

Presently, the model described in this section is being modified to take into account other forces on the bubble, such as those induced by current carrying conductors. In this way, the current-access ion-implanted device described in the previous section may be modelled. Recall that the computer simulations of the previous section were basically for the *static* characteristics of the hybrid device, such as the bubble collapse field. However, with the model introduced in this section, we may predict bubble motion in the hybrid structure as was done for the ion-implanted device.

Figure 13: Bubble position as a function of drive field position around an unimplanted disc for two different values of the normalized drive field, h assuming an isotropic material.

References

1. Ohta, H. and Kryder, M.H. "Current-access ion-implanted bubble device structure", *J. Appl. Phys.*, **53** (3), March 1982, pp. 2531-2533

2. Walsh, T. *Magnetic Bubble Propagation Using Distributed Electric Currents* Ph.D. Dissertation, Carnegie Mellon University, 1975

3. Walsh, T. and Charap, S.H. "Novel Bubble Drive", *A.I.P. Conference Proceedings*. No. 24, 1974 pp. 550-551

4. Bobeck, A.H., Blank, S.L., Butherus, A.D., Ciak, F.J., and Strauss, W. " Current Access Magnetic Bubble Circuits", *The Bell System Technical Journal*, Vol. 58, No. 6, July-August 1979

5. Copeland, J.A., Elward, J.P., Johnson, W.A. and Ruch, J.G. "Single-Conductor Magnetic Bubble Propagation Circuits", *J. Appl. Phys.*, Vol. 42, No. 4, March 1971, pp. 1266-1267

6. Keister, B.D. and Smith, R.L. "A Multiple Scattering Theory for Current-Access Magnetic Bubbles" To be published

7. Calhoun, B.A. *IEEE Trans. Magn.*, MAG-18, 1373-1375 (1982)

8. Keezer, D.C. Thesis, Carnegie Mellon University, (1983)

9. Argyle, B.E., Kryder, M.H., Mundie, R.E. and Slonczewski, J.C. *IEEE Trans. Magn.*, MAG-14, 593 (1978)

10. Greenberg, Michael D. in *Foundations of Applied Mathematics* Prentice-Hall Englewood Cliffs, NJ (1978)

List of Figures

INTEGRATION OF SEMICONDUCTOR
AND
MAGNETIC BUBBLE DEVICES SOI ON GARNET

D.W. GREVE, M.H. KRYDER, AND P.H.L. RASKY
Carnegie- Mellon University, Dept of Electrical and Computer Engineering,
Schenley Park, Pittsburgh, PA 15213

ABSTRACT

Silicon on insulator (SOI) technology makes it possible to fabricate semiconductor devices on foreign substrates. In this paper, we present results for a process in which field effect transistors are fabricated in recrystallized polysilicon on a magnetic bubble substrate. We report on the characteristics of the field effect transistors and the effect of the necessary processing steps on the magnetic properties of the substrate A memory constructed in this hybrid technology would have very high density, multiple detectors for high speed, and direct logic level outputs.

INTRODUCTION

Fabrication of semiconductor devices on the same substrate as magnetic bubble memory structures offers a number of potential advantages In current production technology, bubbles are detected by a magnetoresistive detector which occupies a considerable fraction of the chip area (~5%) The access time is limited by the rate at which bubbles can be moved past this detector Unlike semiconductor memories, parallel outputs are not practical because of the large area required for each detector In addition, the sensitivity of the detector is low resulting in the need for sensitive off-chip amplifier circuitry [1,2]

Bubble memories have the advantages of nonvolatility and relative immunity to environmental stresses We are working to improve the performance of magnetic bubble memories by replacing magnetoresistive detectors with semiconductor detectors which are smaller and more sensitive In addition, we believe that on- chip amplifiers can be produced which will drive loads at standard logic levels We therefore seek to fabricate working semiconductor devices on bubble substrates without damaging the magnetic properties of the substrate underneath

In our present technology, laser recrystallization is used to convert small grain polysilicon into large grain material which can then be used to make MOSFETs and magnetic detectors To date, we have demonstrated

END
3-87
DTIC